



OPEN ACCESS

EDITED BY

Yanxia Zhang,
National Astronomical Observatories
(CAS), China

REVIEWED BY

Alex Lazarian,
University of Wisconsin-Madison,
United States
Vladimir A. Sreckovic,
University of Belgrade, Serbia

*CORRESPONDENCE

Le Ngoc Tram,
nle@mpifr-bonn.mpg.de
Thiem Hoang,
thiemhoang@kasi.re.kr

SPECIALTY SECTION

This article was submitted to
Astrostatistics,
a section of the journal
Frontiers in Astronomy and Space
Sciences

RECEIVED 19 April 2022

ACCEPTED 29 August 2022

PUBLISHED 07 October 2022

CITATION

Tram LN and Hoang T (2022), Recent
progress in theory and observational
study of dust grain alignment and
rotational disruption in star-
forming regions.
Front. Astron. Space Sci. 9:923927.
doi: 10.3389/fspas.2022.923927

COPYRIGHT

© 2022 Tram and Hoang. This is an
open-access article distributed under
the terms of the [Creative Commons
Attribution License \(CC BY\)](https://creativecommons.org/licenses/by/4.0/). The use,
distribution or reproduction in other
forums is permitted, provided the
original author(s) and the copyright
owner(s) are credited and that the
original publication in this journal is
cited, in accordance with accepted
academic practice. No use, distribution
or reproduction is permitted which does
not comply with these terms.

Recent progress in theory and observational study of dust grain alignment and rotational disruption in star-forming regions

Le Ngoc Tram^{1*} and Thiem Hoang^{2,3*}

¹Max-Planck-Institut für Radioastronomie, Bonn, Germany, ²Korea Astronomy and Space Science Institute, Daejeon, South Korea, ³Korea University of Science and Technology, Daejeon, South Korea

Modern understanding of dust astrophysics reveals that radiative torques (RATs) arising from the radiation–dust interaction can induce two fundamental effects: grain alignment and rotational disruption. Here, we review the recent progress in the theoretical development and observational testing of these effects using dust polarization observed toward star-forming regions (SFRs). We first review the basic theory of the RAT alignment and RAT disruption, which are referred to as RAT-A and RAT-D effects, respectively. We then briefly describe the numerical method used to model polarized thermal dust emission by accounting for both RAT-A and RAT-D and theoretical predictions of dust polarization for observations. Next, we review our observational efforts to search for observational evidence of the RAT-A and RAT-D effects using thermal dust polarization toward SFRs. Finally, we discuss magnetic fields inferred from dust polarization observed toward these SFRs and implications of the RAT paradigm for different astrophysical conditions, including protostellar environments, dust evolution, and time-domain astrophysics.

KEYWORDS

interstellar medium, astrophysical dust processes, interstellar dust, interstellar dust extinction, dust continuum emission, starlight polarization, interstellar magnetic fields, star formation

1 Introduction

Dust is an essential component of the interstellar medium (ISM) and plays an important role in many astrophysical phenomena, from ISM evolution, star formation, and planet formation to surface chemistry. The dust properties, including the size, shape, and composition, determine the extinction of starlight and re-emission in infrared emission, which control the appearance of the Universe (Draine, 2011). Thermal dust emission is at the foundation of infrared, submm/mm astronomy, a central topic which is the formation process of stars and planets. In particular, the discovery of starlight polarization (Hall, 1949; Hiltner, 1949) revealed that dust grains are non-spherical

and aligned with a preferred direction in space, which demonstrated the existence of the interstellar magnetic field.

A magnetic field is believed to play an important role in various astrophysical phenomena, including the evolution of the ISM, star formation (Crutcher, 2012), and cosmic ray acceleration and transport. Therefore, observations of the magnetic field have important implications for understanding astrophysical phenomena. Motivated by the discovery of starlight polarization and grain alignment, Davis (1951) and Chandrasekhar and Fermi (1953) introduced a technique to measure the field strength using dust polarization orientations, which is based on the energy balance between turbulent energy and magnetic energy (known as DCF technique). Hildebrand (1988) realized that polarization of far-IR thermal emission from dust grains aligned with the magnetic field can be used to trace the field morphology in very cold regions where young stars are being formed because long-wavelength photons can propagate a long distance. These enabled the rapid development of far-IR/submm polarimetric capabilities in the last decades, including SMA (Marrone and Rao 2008), CSO/SHARP (Li et al., 2008), Planck (Planck Collaboration et al., 2014), BLAST-Pol (Galitzki et al., 2014), PILOT (Misawa et al., 2014), APEX/POLKA (Wiesemeyer et al., 2014), CARMA (Hull and Plambeck, 2015), ALMA (Nagai et al., 2016), JCMT/POL2 (Friberg et al., 2018), and SOFIA/HAWC+ (Harper et al., 2018). As a result, significant progress in understanding the role of magnetic fields in the interstellar process has been made, from diffuse interstellar clouds (e.g., Heiles and Crutcher 2005; Planck Collaboration et al., 2015) and star-forming regions (e.g., Curran and Chrysostomou, 2007; Chuss et al., 2019; Doi et al., 2020; Arzoumanian et al., 2021; Devaraj et al., 2021; Guerra et al., 2021; Kwon et al., 2022, see also Pattle et al., 2022 for reviews) to extra-galactic scales (e.g., Jones et al., 2020; Lopez-Rodriguez et al., 2020; Borlaff et al., 2021; Lopez-Rodriguez 2021; Pattle et al., 2021a).

However, questions of how dust grains get aligned and whether dust polarization is a reliable tracer of magnetic field are long-standing questions in astrophysics (see Lazarian, 2007 for a review). In principle, the process of grain alignment includes two stages: 1) the alignment of the grain axis of maximum inertia moment (i.e., the shortest axis) with its angular momentum (the so-called internal alignment) and 2) the alignment of the grain angular momentum with a preferred axis in space (i.e., axis of grain alignment), which includes the external magnetic field and radiation direction (so-called external alignment). The leading process for the internal alignment of interstellar grains is the Barnett relaxation effect (Barnett, 1909; Purcell, 1979). The Barnett effect is the reverse of the Einstein–de Haas effect (Einstein and de Haas 1915), arising from the dissipation of grain rotational energy into heat due to rotating magnetization within a paramagnetic grain rotating around a non-principal axis.

For the ISM (e.g., the diffuse ISM and molecular clouds (MCs)) where grains are essentially small (of radius of $a < 1 \mu\text{m}$),

the Barnett relaxation is usually much faster than the randomization of grain orientation by gas collisions, resulting in the perfect internal grain alignment (i.e., the grain axis of maximum inertia moment is parallel to its angular momentum; see e.g., Hoang, 2022). For external alignment, the leading theory of grain alignment is based on radiative torques (hereafter RATs, Dolginov and Mitrofanov, 1976; Draine and Weingartner, 1996; Lazarian and Hoang, 2007a) and/or mechanical torques (METs; Lazarian and Hoang 2007b; Hoang et al., 2018). Many predictions of the RAT alignment (or RAT-A) theory were successfully tested with observations (Andersson et al., 2015). The fast Larmor precession establishes the magnetic field as a preferred axis of external alignment (see e.g., Hoang, 2022). Therefore, dust polarization is an established, reliable tracer of magnetic fields in such conditions, which is the focus of this review.

Yet, for special environments where the radiation intensity is strong while the magnetic field is weak or grain susceptibility is negligible (e.g., carbonaceous dust), or the gas is very dense (e.g., protostellar cores/disks and protoplanetary disks, in which grains could grow to very large size of $> 10 \mu\text{m}$), the physics of grain alignment becomes more complex. For example, large grains may be aligned with the radiation direction instead of the magnetic field, as originally suggested in Lazarian and Hoang (2007a) and modeled in Tazaki et al. (2017) and Pattle et al. (2021b). As a result, it is not clear whether dust polarization can still trace magnetic fields in such very dense environments. A detailed study of grain alignment for large grains in protostellar environments is presented in Hoang T. et al. (2022).

While dust polarization orientations have become a powerful method to measure the magnetic field, the dust polarization degree (p) provides a unique probe into dust properties and dust fundamental physics. Indeed, the degree of dust polarization depends on the grain alignment efficiency, grain properties, local density, and magnetic field structure (e.g., Draine and Fraisse, 2009; Guillet et al., 2018). According to the RAT-A theory, the alignment efficiency of dust grains depends on local conditions such as gas properties and radiation (Hoang et al., 2021b) and grains' geometric properties (size and shape) and magnetic properties (Lazarian and Hoang, 2007a; Hoang and Lazarian, 2008, 2016a; Herranen et al., 2021). Therefore, p allows to probe physics of grain alignment and physical properties of dust grains such as grain sizes and composition. The variation of p with the total emission intensity (I) permits a popular analysis of polarimetric data to study the variation of grain alignment and magnetic field geometry across the observed region. The general trend observed toward molecular clouds is $p \propto I^{-\alpha}$ with the power-index α between 0 and 1 (e.g., Coudé et al., 2019; Pattle et al., 2019; Ngoc et al., 2021). If the magnetic field is uniform, $\alpha = 0$, indicating that grain alignment is uniform, whereas $\alpha = 1$ implies that grain alignment only occurs in the outer layer of the cloud and becomes completely lost in the inner region (Whittet et al., 2008). If magnetic fields are completely random, the uniform grain alignment results in a slope of $\alpha \approx 0.5$ (see Jones et al., 1992, 2015).

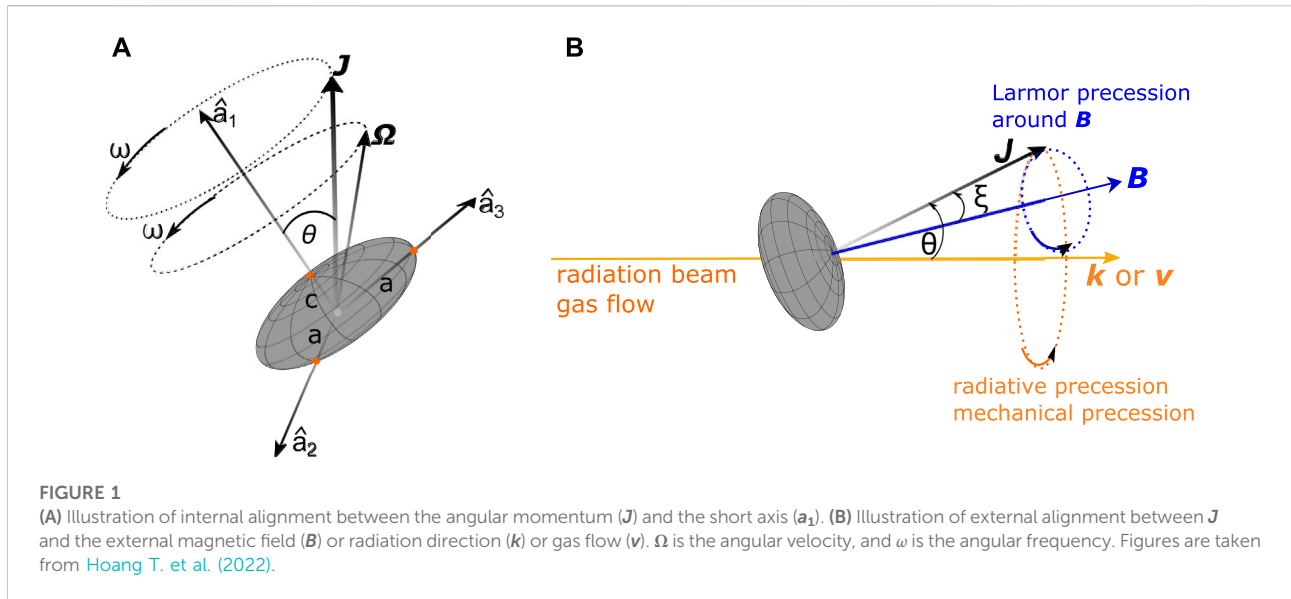
Nevertheless, the $p - I$ relation is not a perfect tracer of grain alignment because of the complex dependence of the emission intensity on the gas density and dust properties. Indeed, the total emission intensity observed at frequency ν is $I_\nu \propto B(T_d)\tau_\nu \sim f_{dg} N_H \times B(T_d) \times \kappa_\nu$, where f_{dg} is the dust-to-gas mass ratio and κ_ν is the dust opacity, which is the product of gas column density (N_H), dust temperature (T_d), and dust opacity (i.e., grain size distribution and composition) along the line of sight. Therefore, the $p - I$ relation reflects the overall dependence of p on the product of three key parameters (gas density, radiation field, and grain size distribution). To disentangle the effect of the radiation field from the gas density, it is required to analyze the variation of the polarization degree with the dust temperature and the gas column density. The first analysis directly reveals the grain alignment by RATs, whereas the second one reflects the effect of grain randomization induced by gas collisions. The dust polarization is predicted to increase with radiation emission intensity (or T_d) by theory (Hoang et al., 2021b), numerical modeling (Lee et al., 2020), and numerical simulations (Reissl et al., 2016). A detailed analysis of the polarization data for various clouds by Planck Collaboration et al. (2020) shows that the polarization degree at $850 \mu\text{m}$ decreases with dust temperature for $T_d \geq 19 \text{ K}$ (see their Figure 18). This observed feature challenges the classical picture of the RAT-A theory.

Recently, a new fundamental effect induced by RATs, namely, radiative torque disruption (or RAT-D), has been realized by Hoang et al. (2019); Hoang (2019). The effect is based on the fact that an irregular dust grain exposed to a strong radiation field could be disrupted into small fragments when the centrifugal stress induced by suprathermal rotation by RATs exceeds the maximum binding energy of the grain material (i.e., tensile strength). Since RATs are stronger for larger grains (Lazarian and Hoang, 2007a; Hoang and Lazarian, 2008), RAT-D is effective for large grains, which then determines the upper cutoff of the grain size distribution (GSD) and causes the variation of GSD with the radiation field. The modified GSD by RAT-D, in turn, affects dust optical-UV extinction, thermal emission from infrared to radio wavelengths, and polarization (see Hoang, 2020 for a review). The RAT-D effect has been studied in many astrophysical environments, including extinction curves toward starburst galaxies (Hirashita and Hoang, 2020), light curve of type Ia supernovae (Giang et al., 2020) and gamma-ray burst (GRB) afterglows (Hoang et al., 2020), evolution of ice in protoplanetary disks (Tung and Hoang, 2020) and cometary comae (Hoang and Tung, 2020), circumsolar dust (Hoang et al., 2021a), rotational desorption of interstellar organic molecules (Hoang and Tram, 2020), spinning dust nanoparticles in circumstellar envelopes of evolved stars (Tram et al., 2020), radiation pressure feedback from massive protostars (Hoang, 2021b), and dust evolution across cosmic time (Hoang, 2021a). In particular, Lee et al. (2020) performed numerical modeling of multi-wavelength polarized thermal dust emission from aligned

grains and disruption by RATs in MCs. They showed that the polarization at $850 \mu\text{m}$ first increases and then decreases with T_d , which could reproduce the $p - T_d$ trend observed by Planck (Planck Collaboration et al., 2020). Tram et al. (2021a) carried out a detailed modeling to interpret the $p - T_d$ of Ophiuchus, a cloud observed by SOFIA/HAWC+ with higher resolution than Planck. The authors demonstrated that the combination of the RAT-A and RAT-D effects could successfully reproduce the observational data. Since then, more observations have shown evidences for the RAT-D mechanism (e.g., Tram et al., 2021b; Ngoc et al., 2021; Hoang T. D. et al., 2022).

High-resolution polarimetric observations toward starless cores (e.g., Alves et al., 2014; Jones et al., 2015) and protostars (e.g., Hull et al., 2014; Cox et al., 2018; Pattle and Fissel, 2019) usually report the decrease of the polarization degree with increasing column density or intensity of dust emission, also known as “polarization hole”. Moreover, two popular reasons proposed to explain the polarization hole includes the decrease of grain alignment efficiency toward denser gas/lower radiation fields and the tangling of the magnetic field (Goodman et al., 1992, 1995; Hull et al., 2014). In the case of protostars, one expects, however, an increase of grain alignment efficiency toward the protostar due to the increasing incident radiation flux in accordance with the RAT-A theory. Hence, an increase in the induced polarization degree is expected in proximity to the peak intensity. Therefore, the underlying origin of the polarization hole toward protostars is difficult to understand and reconcile in terms of grain alignment theory. The mismatch between theory and observations has been reported in Pillai et al. (2020) and Zielinski et al. (2021). Hoang et al. (2021b) showed that the rotational disruption by RATs could occur in the vicinity of protostars and suggested the combination of grain alignment and disruption by RATs as a plausible origin of the polarization hole. For MCs without embedded sources or line of sights far away from the source, the polarization hole may be dominated by the effect of B-field tangling and grain alignment loss (see Pattle and Fissel, 2019).

In this review, we summarize the fundamentals of grain alignment in the context of suprathermal rotation and disruption by RATs and internal and external alignment processes within conditions of the molecular cloud in Section 2. In Section 3, we summarize the numerical modeling that predicts the polarized thermal dust emission of molecular cloud irradiated by a nearby luminosity source in the framework of the RAT paradigm (RAT-A and RAT-D effects). We review some representative observational interpretations in Section 4. In Section 5, we discuss grain alignment to trace magnetic fields in molecular clouds and very dense conditions in protostellar cores/disks, including a polarization hole within the RAT paradigm, effects of RAT paradigm in time-domain astrophysics and on grain growth and evolution, and suprathermal rotation induced by mechanical torques.



2 Grain alignment and disruption by radiative torques: The RAT paradigm

2.1 Radiative torques and its fundamental effects

Dolginov and Mitrofanov (1976) first suggested that the interaction of an anisotropic radiation with a helical grain can induce RATs due to the differential scattering/absorption of left- and right-handed circularly polarized photons. Latter, RATs were numerically demonstrated in Draine and Weingartner (1996) for three irregular grain shapes. Lazarian and Hoang (2007a) introduced an analytical model (AMO) of RATs, which is based on a helical grain consisting of an oblate spheroid and a weightless mirror. The AMO is shown to reproduce the basic properties of RATs obtained from numerical calculations for realistically irregular grain shapes (Lazarian and Hoang, 2007a; Hoang and Lazarian, 2008; Herranen et al., 2021), and it enables us to make quantitative predictions for various conditions (Hoang and Lazarian, 2014) and dust compositions (Lazarian and Hoang, 2008; Hoang and Lazarian, 2009, 2016a). Many predictions from the RAT alignment (hereafter RAT-A) theory were observationally tested (see Andersson et al., 2015; Lazarian et al., 2015 for recent reviews).

As shown in previous studies (Draine and Weingartner, 1997; Lazarian and Hoang, 2007a; Hoang and Lazarian, 2008), RATs in general can induce three fundamental effects on grain rotational dynamics: 1) the grain precession around the radiation direction, 2) spin-up the grain to suprathermal rotation as well as spin-down to thermal rotation, and 3) align the grain with \mathbf{J} along the radiation \mathbf{k} .

2.2 Grain model and magnetic properties

2.2.1 Grain model

Let us define an irregular grain of size a and mass density ρ (Figure 1). In the fixed grain's frame, this irregular shape is described by three principal axes $\hat{\mathbf{a}}_1, \hat{\mathbf{a}}_2, \hat{\mathbf{a}}_3$ with the inertia moments of $I_1 > I_2 \geq I_3$, respectively. For the sake of simplicity, we assume an oblate spheroidal shape (i.e., $I_1 > I_2 = I_3$) with the length of the semi-minor axis of c and the lengths of the semi-major axes of a . The corresponding inertial moments are $I_{\parallel} \equiv I_1 = \frac{8\pi}{15} \rho a^4 c = \frac{8\pi}{15} \rho s a^5$ and $I_{\perp} \equiv I_2 = I_3 = \frac{4\pi}{15} \rho a^2 c (a^2 + c^2) = \frac{4\pi}{15} \rho s a^5 (1 + s^2)$, where $s = c/a$ is the axial ratio of oblate grains. This grain volume is $V = 4/3\pi s a^3$.

For an isolated grain, the angular momentum \mathbf{J} is conserved, and the grain axis of maximum inertia in general makes an angle with \mathbf{J} . Figure 1A describes the torque-free motion of the oblate grain, which includes the precession of angular velocity of Ω or momentum \mathbf{J} with a frequency of ω along the grain shortest axis. In the presence of an external magnetic field, radiation field, or a gas flow, the angular momentum \mathbf{J} precesses around the magnetic field, radiation field, or incident gas flow, see Figure 1B (Lazarian and Hoang, 2007a,b).

2.2.2 Grain magnetic properties

Magnetic properties of dust are essential for their interaction with the ambient magnetic field and grain alignment. We consider grains with embedded iron atoms (such as silicate grains). The presence of iron atoms with unpaired electrons makes interstellar dust a natural paramagnetic material. When iron atoms are diffusely distributed, the grain is called paramagnetic (PM). When iron atoms are distributed as iron

clusters, dust grains become superparamagnetic materials (SPM, see [Hoang and Lazarian, 2016a](#)).

The magnetic susceptibility of a paramagnetic grain at rest is given as follows:

$$\chi_{\text{PM}}(0) = 0.03n_{23}f_p\hat{p}^2\left(\frac{20\text{ K}}{T_d}\right), \quad (1)$$

with $\hat{p} = p/5.5$ ($p \approx 5.5$ for silicate grains; see [Hoang and Lazarian, 2016a](#), and references therein). This equation shows the dependence on T_d . The magnetic susceptibility reduces for higher T_d because of the halt in magnetization due to the thermal fluctuation of free-electron spins.

For a superparamagnetic grain, we get the following:

$$\chi_{\text{SPM}}(0) = 0.026N_{\text{cl}}\phi_{\text{sp}}\hat{p}^2\left(\frac{20\text{ K}}{T_d}\right). \quad (2)$$

Here, N_{cl} is the number of Fe atoms per cluster, and ϕ_{sp} is the volume filling factor of iron cluster in grain. N_{cl} could vary from 20 to 10^5 ([Jones and Spitzer, 1967](#)). One can see that iron inclusion significantly increases the magnetic property of grains.

For a grain rotating at a frequency ω , the magnetic susceptibility is a complex number with the imaginary part that describes the absorption properties of magnetic energy, given as follows:

$$\chi_2(\omega) = \frac{\chi(0)\tau_{\text{el}}\omega}{[1 + (\omega\tau_{\text{el}}/2)^2]}, \quad (3)$$

where $\tau_{\text{el}} = 2.9 \times 10^{-12}/f_p n_{23}$ is the spin-spin relaxation time with $n_{23} = n/10^{23} \text{ cm}^{-3}$ being the atomic density of material, and f_p the fraction of Fe atoms in the grain (e.g., $f_p = 1/7$ for MgFeSiO₄ grains, see [Hoang et al., 2014](#)).

Let us define a quantity $K(\omega) = \chi_2(\omega)/\omega$, which yields

$$K_{\text{PM}}(\omega) \approx 8.7 \times 10^{-14}\hat{p}\left(\frac{20\text{ K}}{T_d}\right)\left(\frac{1}{[1 + (\omega\tau_{\text{el}}/2)^2]}\right), \quad (4)$$

and

$$K_{\text{SPM}}(\omega) \approx 2.6 \times 10^{-11}N_{\text{cl}}\phi_{\text{sp}}\hat{p}^2\left(\frac{20\text{ K}}{T_d}\right)k_{\text{SPM}}(\omega), \quad (5)$$

with

$$k_{\text{SPM}}(\omega) = \exp\left(\frac{0.011\text{ K} \times N_{\text{cl}}}{T_d}\right)\left[1 + \left(\frac{\omega\tau_{\text{sp}}}{2}\right)^2\right]^{-2}, \quad (6)$$

where τ_{sp} is the timescale of thermally activated remagnetization, given as follows:

$$\tau_{\text{sp}} \approx 10^{-9} \exp\left(\frac{0.011\text{ K} \times N_{\text{cl}}}{T_d}\right) \text{ s}. \quad (7)$$

The supermagnetic grain has enormously increased magnetic susceptibility ([Jones and Spitzer, 1967](#)), and the coupling with the magnetic field is stronger than in an ordinary paramagnetic

grain. Note that a superparamagnetic grain behaves like a paramagnetic grain in the absence of an external magnetic field.

2.3 Grain suprathreshold rotation by RATs and rotational damping

Let us consider a grain exposed to a radiation field of the energy density of u_{rad} (erg cm^{-3}), a mean wavelength of $\bar{\lambda}$, and an anisotropy degree of γ^l . Its strength is defined by a dimensionless $U = u_{\text{rad}}/u_{\text{ISRF}}$, where $u_{\text{ISRF}} = 8.64 \times 10^{-13} \text{ erg cm}^{-3}$ is the radiation energy density of the interstellar radiation field (ISRF) in the solar neighborhood ([Mathis et al., 1983](#)).

The rotation of an irregular grain of size a is described by the suprathreshold number $St = \Omega/\Omega_T$ with $\Omega_T = (k_B T_{\text{gas}}/I_1)^{0.5}$ the thermal angular velocity. Grain rotation is called ‘‘suprathreshold’’ for $St > 1$ and ‘‘subthreshold’’ for $St < 1$.

One of the important effects of RATs is to spin-up the dust grains of irregular shapes. On the another hand, gas collisions and IR re-emission spin-down the grain. The timescale characterizing the grain rotational damping by gas collisions and IR emission is

$$\tau_{\text{damp}} = \frac{\tau_{\text{gas}}}{1 + F_{\text{IR}}} \quad (8)$$

where τ_{gas} and F_{IR} are the gas collision damping timescale and the ratio of the IR re-emission to collisional damping times, which are

$$\tau_{\text{gas}} = \frac{3}{4\sqrt{\pi}} \frac{I_{\text{vert}}}{1.2n_{\text{H}}m_{\text{H}}v_{\text{T}}a^4\Gamma_1} \approx 8.3 \times 10^3 \hat{\rho} \left(\frac{sa_{-5}}{n_3 T_1^{1/2} \Gamma_1}\right) \text{ yr}, \quad (9)$$

$$F_{\text{IR}} \approx 3.8 \times 10^{-2} \left(\frac{U^{2/3}}{a_{-5}}\right) \left(\frac{10^3 \text{ cm}^{-3}}{n_{\text{H}}}\right) \left(\frac{10\text{ K}}{T_{\text{gas}}}\right)^{1/2}. \quad (10)$$

with $n_3 = n_{\text{H}}/(10^3 \text{ cm}^{-3})$ the gas volume density, $T_1 = T_{\text{gas}}/10\text{ K}$ the gas temperature, $a_{-5} = a/(10^{-5} \text{ cm})$ the grain size, $\hat{\rho} = \rho/(3 \text{ g cm}^{-3})$ the mass density of the grain, and Γ_1 the geometrical parameter ($\Gamma_1 = 1$ for a spherical grain and 0.82 for a grain of axial ratio $s = 1/2$; see [Hoang, 2022](#))

The balance between the spin-up by RATs and spin-down by gas collisions and IR emission establishes the maximum rotation rate of grains due to RATs. For a simple case of a constant luminosity source², the maximum angular velocity that an irregular grain acquired by RATs is

$$\Omega_{\text{RAT}} = \frac{\bar{\Gamma}_{\text{RAT}}\tau_{\text{damp}}}{I_{\parallel}} \quad (11)$$

1 $\gamma = 0$ for an isotropic radiation field, and $\gamma = 1$ for an unidirectional radiation field. For a typical diffuse interstellar radiation field: $\gamma = 0.1$. For molecular cloud: $\gamma \approx 0.7$ ([Draine and Weingartner 1996](#))

2 If the radiation source varies in luminosity, the angular velocity Ω_{RAT} is obtained by solving the equation of motion; see Eq. 12 in [Hoang et al. \(2019\)](#).

where $\bar{\Gamma}_{\text{RAT}}$ is the average RAT acting on grain, which depends on the RAT efficiency (Q_{r}), grain size (a_{eff}) and local radiation ($u_{\text{rad}}, \bar{\lambda}, \gamma$) as

$$\bar{\Gamma}_{\text{RAT}} = \pi a_{\text{eff}}^2 \left(\frac{\bar{\lambda}}{2\pi} \right) \gamma u_{\text{rad}} \bar{Q}_{\text{r}} \quad (12)$$

The RAT efficiency strongly depends on the ratio of radiation wavelength and grain size as $\bar{Q}_{\text{r}} \propto (\lambda/a)^{-\eta_3}$, indicating that RATs could be effective at longer wavelengths for large grains (e.g., optical-IR photons) rather than only UV photons. Thus, the RAT effect is effective in more extended regions than other dust effects induced by UV photons, such as photo-electron emission.

Because the RAT efficiency changes its slope at $a \approx \bar{\lambda}/2.5$, the suprathermal number of grains spun-up by RATs is described separately as (Hoang, 2022)

$$St_{\text{RAT}} \approx 180 \hat{\rho}^{1/2} s^{5/6} a_{-5}^{7/2} \left(\frac{\bar{\lambda}}{1.2 \mu\text{m}} \right)^{-2} \left(\frac{\gamma U}{n_3 T_1} \right) \left(\frac{1}{1 + F_{\text{IR}}} \right), \quad (13)$$

for $a \lesssim \bar{\lambda}/2.5$, and

$$St_{\text{RAT}} \approx 2.1 \times 10^4 \hat{\rho}^{1/2} s^{-1/6} a_{-5}^{1/2} \left(\frac{\bar{\lambda}}{1.2 \mu\text{m}} \right) \left(\frac{\gamma U}{n_3 T_1} \right) \left(\frac{1}{1 + F_{\text{IR}}} \right). \quad (14)$$

for $a > \bar{\lambda}/2.5$.

For regions where the gas density is very high and the radiation strength is rather small (i.e., $F_{\text{IR}} \ll 1$), such as in protostellar cores and the mid-plane of protoplanetary disks, one can see that $St_{\text{RAT}} \propto U/n_3 T_1$. For regions with very strong radiation fields but a low gas density (i.e., $F_{\text{IR}} \gg 1$), such as in the vicinity of a radiation source, one has $St_{\text{RAT}} \propto U^{1/3}$. Note that St_{RAT} also strongly depends on the size of the grains, the bigger grain size, the faster rotation induced by RATs. Therefore, large grains are easily to be spun-up suprathermally in strong radiation fields.

2.4 Internal alignment

The internal alignment describes the alignment of the angular momentum \mathbf{J} with the short axis \mathbf{a}_1 of the grain, as illustrated in Figure 1A. Here, we discuss three relaxation processes that induce internal alignment, including Barnett relaxation, nuclear relaxation, and inelastic relaxation, as well as show the critical grain sizes for each internal alignment.

2.4.1 Barnett relaxation

The most important process relies on the Barnett relaxation (Purcell, 1979). A rotating (super)paramagnetic grain will be magnetized due to the Barnett effect, which results in the dissipation of rotational energy due to the rotating component perpendicular to \mathbf{a}_1 . The dissipation will eventually bring Ω and \mathbf{J}

aligned with \mathbf{a}_1 , which is the minimum energy state. The stage of $\mathbf{J} \perp \mathbf{a}_1$ is called ‘‘right internal alignment’’.

The relaxation times by the Barnett effect for a paramagnetic (so-called Barnett relaxation) and a supermagnetic grain (so-called super-Barnett relaxation) are given as follows:

$$\tau_{\text{BR,PM}} = \frac{\gamma_e^2 I_{\parallel}^3}{V K_{\text{PM}}(\omega) h^2 (h-1) J^2} \approx 0.5 \hat{\rho}^2 a_{-5}^7 f(\hat{s}) \times \left(\frac{J_{\text{d}}}{J} \right)^2 \left[1 + \left(\frac{\omega \tau_{\text{cl}}}{2} \right)^2 \right]^2 \text{ yr}, \quad (15)$$

$$\tau_{\text{BR,SPM}} = \frac{\gamma_e^2 I_{\parallel}^3}{V K_{\text{SPM}}(\omega) h^2 (h-1) J^2} \approx 0.16 \hat{\rho}^2 f(\hat{s}) a_{-5}^7 \times \left(\frac{1}{N_{\text{cl}} \phi_{\text{sp},-2} \hat{\rho}^2} \right) \left(\frac{J_{\text{d}}}{J} \right)^2 \left(\frac{T_{\text{d},1}}{k_{\text{SPM}}(\omega)} \right) \text{ yr}, \quad (16)$$

where $V = 4\pi/3 a^3$ is the grain volume, $\gamma_e = -g_e \mu_B / \hbar$ is the gyromagnetic ratio of an electron ($g_e \approx 2$ and $\mu_B \approx 9.26 \times 10^{-21}$ erg G^{-1}), $\hat{s} = s/0.5$, $f(\hat{s}) = \hat{s} [(1 + \hat{s}^2)/2]^2$, and $J_{\text{d}} = \sqrt{I_{\parallel} k_{\text{B}} T_{\text{d}} / (h-1)}$ is the dust thermal angular momentum (see also Hoang and Lazarian 2014) with $h = I_{\parallel} / I_{\perp} = 2/(1 + s^2)$ and $\phi_{\text{sp},-2} = \phi_{\text{sp}}/0.01$.

However, gas collisions can strongly randomize the internal alignment if the Barnett relaxation is slower than the grain randomization by gas collisions. Therefore, grains have efficient internal alignment when the timescale for the Barnett relaxation is shorter than that for gas rotational damping. Thus, the maximum size that a paramagnetic and superparamagnetic grain has the internal alignment with \mathbf{J} along the short axis \mathbf{a}_1 can be determined by the balance between these two timescales, which yields the following (Hoang T. et al., 2022):

$$a_{\text{max,a1}}^{\text{PM}} \approx 0.39 \times h^{1/3} St^{1/3} \left(\frac{\hat{\rho}^2}{\hat{\rho} n_3 T_1^{1/2}} \right)^{1/6} \times \left(\frac{1}{1 + (\omega \tau_{\text{tel}}/2)^2} \right)^{1/3} \left(\frac{(h-1) T_{\text{gas}}}{T_{\text{d}}} \right)^{1/6} \mu\text{m} \quad (17)$$

and

$$a_{\text{max,a1}}^{\text{SPM}} \approx 2.18 h^{1/3} St^{1/3} \left(\frac{N_{\text{cl},4} \phi_{\text{sp},-2} \hat{\rho}^2}{\hat{\rho} n_3 T_1^{1/2} \Gamma_{\parallel}} \right)^{1/6} \times \left(\frac{1}{k_{\text{SPM}}(\omega)} \right)^{1/6} \times \left(\frac{(h-1) T_{\text{gas}}}{T_{\text{d}}} \right)^{1/6} \mu\text{m},$$

where $N_{\text{cl},4} = N_{\text{cl}}/10^4$ (Hoang T. et al., 2022). One can see that $a_{\text{max,a1}}$ increases with grain rotation as $St^{1/3}$ and decreases with gas density as $\sim n_{\text{H}}^{-1/6}$. With iron inclusions, superparamagnetic grains could achieve efficient internal alignment for larger grain sizes.

2.4.2 Nuclear relaxation

Atomic nuclei within the grain can also have nuclear paramagnetism due to unpaired protons and nucleons. The attachment of H atoms to the grain or water ice mantle induces nuclear magnetism due to proton spin (Purcell, 1979). Nuclear paramagnetism can also induce internal relaxation as the Barnett effect for electron spins (Lazarian and Draine, 1999). The nuclear relaxation (NR) time is given by

3 The power index η describes the changes in RAT efficiency with respect to grain size; see Figure 1 in Hoang et al. (2021b).

$$\begin{aligned}\tau_{\text{NR}} &= \frac{\gamma_n^2 I_{\parallel}^3}{VK_n(\omega)h^2(h-1)J^2}, \\ &\approx 125\rho^2 a_{-5}^7 f(\dot{s}) \left(\frac{n_e}{n_n}\right) \left(\frac{J_d}{J}\right)^2 \left(\frac{g_n}{3.1}\right)^2 \left(\frac{2.79\mu_n}{\mu_n}\right)^2 \\ &\quad \times \left[1 + \left(\frac{\omega\tau_n}{2}\right)^2\right]^2, \quad (18)\end{aligned}$$

where γ_n is nuclear gyromagnetic ratio, n_e is the number density of unpaired electrons in the dust, n_n is the number density of nuclei that has the magnetic moment μ_n , and $\mu_n = e\hbar/2m_p c = 5.05 \times 10^{-24}$ erg G $^{-1}$, where m_p is the proton mass is the nuclear magneton, $\tau_n \sim 10^{-5} (3.1/g_n)^2 (10^{22} \text{ cm}^{-3}/n_e)$ s is the nuclear spin-spin relaxation time, and $K_n = \chi_n/\omega$ with χ_n the nuclear magnetic susceptibility (see Hoang, 2022).

The maximum size for internal alignment induced by nuclear relaxation is given by Hoang (2022), as follows:

$$\begin{aligned}a_{\text{max,aj}}(\text{NR}) &< 3.03h^{1/3}St^{1/3} \left(\frac{(n_e/n_n)(g_n/3.1)^2}{n_3 T_1^{1/2} \Gamma_{\parallel}}\right)^{1/6} \\ &\quad \times \left(\frac{1}{1 + (\omega\tau_n/2)^2}\right)^{1/3} \\ &\quad \times \left(\frac{(h-1)T_{\text{gas}}}{T_d}\right)^{1/6} \mu\text{m}. \quad (19)\end{aligned}$$

It increases with the suprathermal rotation as $St^{1/3}$ for $\omega < 2/\tau_n$, but decreases as $St^{-1/3}$ for $\omega > 2/\tau_n$ due to suppression of nuclear magnetism at fast rotation. For the typical density of $n = 10^3 \text{ cm}^{-3}$, large grains of size upto $a \sim 3 \mu\text{m}$ can have efficient internal alignment by nuclear relaxation.

2.4.3 Inelastic relaxation

Atoms and molecules in a rotating grain experience a centrifugal force that stresses them out from the grain central of mass. The chemical attractive forces, on the other hand, tend to tight them together. These effects cause the grain deformation. If grains are made up inelastic materials, the deformation results in the dissipation of rotational energy, which eventually brings the angular momentum J to align with the grain's shortest axis \mathbf{a}_1 (see Purcell, 1979; Lazarian and Efroimsky, 1999). This internal alignment mechanism is named as inelastic relaxation.

The characteristic time of inelastic relaxation for an oblate spheroidal grain can be estimated as follows (see Hoang T. et al., 2022):

$$\begin{aligned}\tau_{\text{iER}} &= \frac{\mu Q}{\rho a^2 \Omega_0^3} g(s) = \frac{\rho^{1/2} a^{11/2} \mu Q}{(kT_{\text{gas}})^{3/2} St^3} g'(s) \\ &= 0.034 \rho^{1/2} a_{-5}^{11/2} \mu_8 Q_3 \frac{g'(s)}{T_1^{3/2} St^3} \text{ yr}, \quad (20)\end{aligned}$$

where Q is the quality factor of grain material ($Q = 100$ for a silicate rocks, Efroimsky and Lazarian 2000), μ is the modulus of rigidity ($\mu \sim 10^7$ erg cm $^{-3}$ for cometary, Knapmeyer et al., 2018). $\Omega_0 = St\Omega_T$, $\mu_8 = \mu/(10^8 \text{ erg cm}^3)$, $Q_3 = Q/10^3$, and $g' = 2.2s^{3/2}g(s)$ with $g(s)$ the geometrical factor as follows:

$$g(s) = \frac{2^{3/2}7}{8} \frac{(1+s^2)^4}{s^4 + 1/(1+\sigma)}, \quad (21)$$

which corresponds to $g(s) = 7.0$ and 4.6 for $s = 1/2$ and $1/3$, respectively.

Following Hoang et al. (2022a), the maximum grain size for efficient inelastic relaxation is defined by $\tau_{\text{iER}} = \tau_{\text{gas}}$ and given by

$$\begin{aligned}a_{\text{max,aj}}(\text{iER}) &\approx 1.55 \left(\frac{\mu_8 Q_3}{\sqrt{\rho}}\right)^{-2/9} \left(\frac{T_1}{n_8}\right)^{2/9} \\ &\quad \times \left(\frac{s}{g'(s)\Gamma_{\parallel}}\right)^{2/9} St^{2/3} \mu\text{m}, \quad (22)\end{aligned}$$

which implies that large grains of $a \sim 1.55 \mu\text{m}$ can be efficiently aligned via inelastic relaxation even at thermal rotation of $St = 1$, and large grains can be aligned for $St > 1$.

Figure 2 shows the comparison of grains having internal alignment by Barnett relaxation for superparamagnetic grains (color lines) and inelastic relaxation (black lines) as functions of the gas density. Grains are assumed to be spun-up by RATs. First, the Barnett relaxation is not effective in very dense regions (e.g., $n_{\text{H}} > 10^9 \text{ cm}^{-3}$) because of the gas rotational damping and lower St_{RAT} . For a given gas density, one can see that Barnett relaxation is more efficient, but the inelastic relaxation is able to align larger grains (panel (a)). The reason is that the maximum grain size for inelastic relaxation scales as $\sim St^{2/3}$, whereas it scales as $\sim St^{1/3}$ for Barnett relaxation. For stronger radiation fields, the inelastic relaxation is efficient in denser gas (panel (b)), which is due to the fact that inelastic timescale reduces as $\sim St^{-1/3}$.

For a typical density of the ISM ($n_{\text{H}} \approx 10^3 \text{ cm}^{-3}$), one can see that the Barnett relaxation for PM/SPM grains are much more effective than the inelastic relaxation. However, unlike the PM/SPM, diamagnetic grains (e.g., carbonaceous dust) does not experience the Barnett relaxation effect, but they could still have efficient internal alignment for size $a < a_{\text{max,aj}}(\text{iER})$ due to inelastic relaxation, because this relaxation is independent from the grain magnetic properties.

2.5 External alignment

The external alignment describes the alignment of the grain angular momentum J with a preferred direction in space, which can be the ambient magnetic field or the radiation direction (see Figure 1B).

2.5.1 Alignment with magnetic fields (magnetic alignment): Larmor precession and magnetic relaxation

2.5.1.1 Larmor precession

The interaction between the grain magnetic moment due to the Barnett effect with the magnetic field induces the Larmor precession of J around B , resulting the first coupling of the grain with the magnetic field (see e.g., Hoang, 2022).

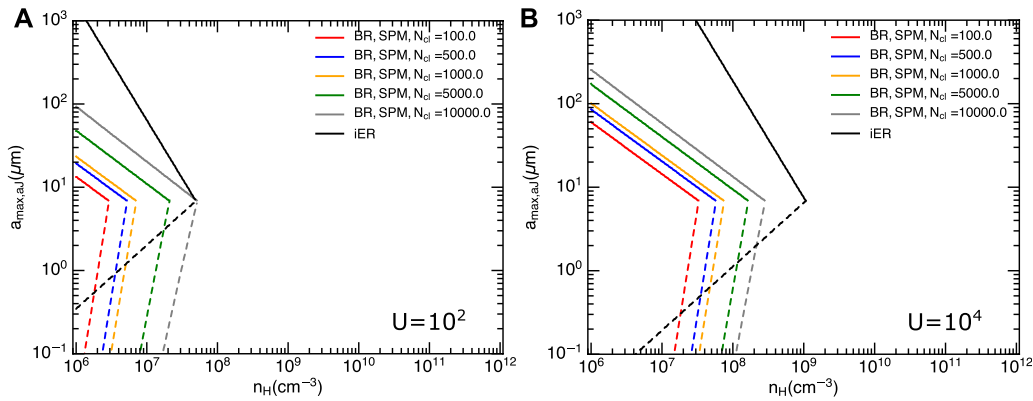


FIGURE 2

Comparison of minimum (dashed line) and maximum (solid line) size of grains having internal alignment by Barnett relaxation (BR) for superparamagnetic grain (SPM, color lines) and inelastic mechanism (iER, black lines) with respect to a large range of gas density (figure adopted from Hoang T. et al., 2022). The grains are spun-up by RATs with $U = 10^2$ (A) and $U = 10^4$ (B).

The rate of the Larmor precession for (super)paramagnetic grains are respectively given by

$$\tau_{B,\text{PM}} = \frac{2\pi}{|d\phi/dt|} = \frac{2\pi I_{\parallel} \Omega}{|\mu_{\text{Bar}}| B} = \frac{2\pi |y_e| I_{\parallel}}{\chi_{\text{PM}}(0) V B} \approx 3.5 \times 10^{-4} \frac{\hat{\rho} T_{d,1} a_{-5}^2}{n_{23} f_p \hat{P}^2} \left(\frac{B}{20 \mu\text{G}} \right)^{-1} \text{ yr}, \quad (23)$$

and

$$\tau_{B,\text{SPM}} = \frac{2\pi |y_e| I_{\parallel}}{\chi_{\text{SPM}}(0) V B} \approx 4.05 \times 10^{-2} \times \frac{\hat{\rho} T_{d,1} a_{-5}^2}{N_{\text{cl}} \phi_{\text{sp},-2} \hat{P}^2} \left(\frac{B}{20 \mu\text{G}} \right)^{-1} \text{ yr}. \quad (24)$$

When the Larmor precession is faster than the gas randomization, the magnetic field becomes an axis of grain alignment, which is known as *magnetic alignment*. The maximum size for the fast Larmor precession around the B-field is defined by $\tau_B = \tau_{\text{gas}}$, which is

$$a_{\text{max,JB}}^{\text{Lar,PM}} \approx 1.2 \times 10^6 \hat{s} n_3^{-1} T_1^{-1/2} T_{d,1}^{-1} \left(\frac{B}{20 \mu\text{G}} \right) \left(\frac{n_{23} f_p \hat{P}^2}{\Gamma_{\parallel}} \right) \mu\text{m}, \quad (25)$$

and

$$a_{\text{max,JB}}^{\text{Lar,SPM}} \approx 1.02 \times 10^9 \hat{s} n_3^{-1} T_1^{-1/2} T_{d,1}^{-1} \left(\frac{B}{20 \mu\text{G}} \right) \times \left(\frac{N_{\text{cl},4} \phi_{\text{sp},-2} \hat{P}^2}{\Gamma_{\parallel}} \right) \mu\text{m}. \quad (26)$$

for PM and SPM grains, respectively.

2.5.1.2 Para- and superparamagnetic relaxation

The angle between J and the magnetic field can be reduced by paramagnetic relaxation, resulting in the magnetic alignment of J

with B . This mechanism is known as the DG relaxation (Davis and Greenstein, 1951). As numerically shown in Hoang and Lazarian (2016a,b), magnetic relaxation alone is not enough to produce efficient grain alignment when grains have thermal rotation (i.e., $St \leq 1$) due to strong internal thermal fluctuations and gas randomization. Yet, the joint action of suprathermal rotation by RATs and magnetic relaxation however can make grains to achieve high degree of alignment.

The characteristic times of the DG relaxation for the PM and SPM grains are given by (see e.g., Hoang and Lazarian, 2016a)

$$\tau_{\text{mag,PM}} = \frac{I_{\parallel}}{V K_{\text{PM}}(\Omega) B^2} = \frac{2\rho a^2}{5K_{\text{PM}}(\Omega) B^2} \approx 8.6 \times 10^4 \frac{\hat{\rho} a_{-5}^2 T_{d,1}}{\hat{P}} \left(\frac{B}{20 \mu\text{G}} \right)^{-2} (1 + (\omega\tau_{\text{cl}}/2)^2)^2 \text{ yr}, \quad (27)$$

and

$$\tau_{\text{mag,SPM}} = \frac{2\rho a^2}{5K_{\text{SPM}}(\Omega) B^2} \approx 3.75 \times 10^2 \frac{\hat{\rho} a_{-5}^2 T_{d,1}}{N_{\text{cl}} \phi_{\text{sp},-2} \hat{P}^2} \frac{T_{d,1}}{k_{\text{SPM}}(\Omega)} \left(\frac{B}{20 \mu\text{G}} \right)^{-2} \text{ yr}. \quad (28)$$

The respective maximum of size that grain alignment can still be affected by the DG magnetic relaxation is defined by $\tau_{\text{mag}} = \tau_{\text{gas}}$ and is equal to (Hoang T. et al., 2022)

$$a_{\text{max,JB}}^{\text{DG,PM}} \approx 0.0097 \times n_3^{-1} T_1^{-1/2} T_{d,1}^{-1} \left(\frac{B}{20 \mu\text{G}} \right)^2 \times (1 + (\omega\tau_{\text{cl}}/2)^2)^{-2} \mu\text{m}, \quad (29)$$

and

$$a_{\text{max,JB}}^{\text{DG,SPM}} \approx 224 \times n_3^{-1} T_1^{-1/2} T_{d,1}^{-1} \left(\frac{B}{20 \mu\text{G}} \right)^2 \frac{N_{\text{cl},4} \phi_{\text{sp},-2} \hat{P}^2}{\hat{\rho}} \mu\text{m}. \quad (30)$$

One can see that the gas density and B-field strength determine which grains are aligned with B-field as $a_{\text{max},\text{JB}}^{\text{DG}} \sim n_{\text{H}}^{-1} B^2$. The DG efficiency drops dramatically with increasing the gas density. Paramagnetic relaxation is negligible for large grains, but superparamagnetic relaxation can be efficient even for large grains up to $\sim 20 \mu\text{m}$ for MCs with $n_{\text{H}} \sim 10^3 \text{ cm}^{-3}$.

2.5.2 The RAT alignment paradigm

Here, we describe the basic elements of the RAT alignment paradigm, including radiative precession, grain alignment at low- J and high- J attractors, and the minimum size for RAT alignment.

2.5.2.1 Radiative precession

In the presence of an anisotropic radiation field, irregular grains experience radiative precession due to RATs, with the grain angular momentum precessing around the radiation direction (\mathbf{k}). For a grain with angular momentum J , the radiative precession time is given by (Lazarian and Hoang, 2007a; Hoang and Lazarian, 2014),

$$\tau_k = \frac{2\pi}{|d\phi/dt|} \approx \frac{2\pi J}{\gamma u_{\text{rad}} a_{\text{eff}}^2 Q_{e3}} \quad (31)$$

$$\approx 56.8 \hat{\rho}^{1/2} T_1^{1/2} \hat{s}^{-1/6} a_{-5}^{1/2} St \left(\frac{1.2 \mu\text{m}}{\gamma \bar{\lambda} \bar{Q}_{e3} U} \right) \text{yr},$$

where $\hat{Q}_{e3} = Q_{e3}/10^{-2}$ with Q_{e3} the third component of RATs that induces the grain precession around \mathbf{k} and the normalization is done using the typical value of Q_{e3} (see Lazarian and Hoang, 2007a).

In the absence of magnetic field, radiative precession can be much faster than gas damping time for a thermal rotation of $St \sim 1$ (Eq. 11). In this case, the anisotropic radiation direction is the axis of grain alignment, which is known as k-RAT alignment.

Low- J and high- J Attractor Alignment by RATs: In addition to radiative precession, RATs can align grains at high- J attractors and low- J attractors. In general, a fraction of grains ($f_{\text{high-}J}$) can be aligned at a high- J attractor due to the aligning and spin-up effects of RATs (Lazarian and Hoang, 2007a; Hoang and Lazarian, 2008). Grains aligned at the high- J attractor have the suprathermal rotation with $St_{\text{high-}J} > 1$. On the other hand, due to the aligning and spin-down effects of RATs, the $1 - f_{\text{high-}J}$ fraction of grains, are aligned at the low- J attractor with $St_{\text{low-}J} \sim 1$ (Hoang and Lazarian, 2014). The RAT alignment process can occur on a timescale smaller than the gas damping time, which is called *fast* alignment (Lazarian and Hoang, 2007a, 2021) with a strong radiation field. Grains can be stably aligned at low- J attractors when the grain randomization by gas collisions is not considered. Otherwise, the gas randomization could randomize grains at low- J attractors and eventually transport them to the high- J attractor after a timescale greater than the gas damping time, which is usually called *slow* alignment (Hoang and Lazarian, 2008; Lazarian and Hoang, 2021). The *fast* RAT alignment occurs in the local environment of intense transient

radiation sources such as supernova (Giang et al., 2020), kilonova, and gamma-ray bursts (Hoang et al., 2020), whereas the *slow* RAT alignment occurs in most astrophysical environments, from the ISM, MCs, to SFRs. A detailed discussion of fast and slow alignment by RATs is discussed in detail in Lazarian and Hoang (2021).

The exact value of $f_{\text{high-}J}$ depends on the grain properties (shape and size) and magnetic susceptibility. For grains with ordinary paramagnetic material (e.g., silicate), Herranen et al. (2021) found that $f_{\text{high-}J}$ can be about 10–70% based on calculations of RATs for an ensemble of Gaussian random shapes. The presence of iron inclusions embedded in the grains increases grain magnetic susceptibility and superparamagnetic relaxation, which can produce in the universal high- J attractors (i.e., $f_{\text{high-}J} \sim 100\%$) (Hoang and Lazarian, 2016a; Lazarian and Hoang, 2021).

2.5.2.2 Minimum size of RAT alignment

Due to gas collisions, grains can be efficiently aligned only when they rotate suprathermally at a high- J attractor. Hoang and Lazarian (2008) and Hoang and Lazarian (2014) demonstrated that grain alignment is stabilized under the gas randomization when $\Omega_{\text{RAT}} \equiv 3 \times \Omega_{\text{T}}$ (or $St_{\text{RAT}} = 3$). This criteria yields the minimum size for grain alignment by RATs as

$$a_{\text{align}} \approx 0.055 \hat{\rho}^{-1/7} \left(\frac{n_3 T_1}{\gamma_{-1} U} \right)^{2/7} \times \left(\frac{\bar{\lambda}}{1.2 \mu\text{m}} \right)^{4/7} \left(\frac{1}{1 + F_{\text{IR}}} \right)^{-2/7} \mu\text{m}, \quad (32)$$

where $\gamma_{-1} = \gamma/10^{-1}$. One can see that for a typical MC with $n_{\text{H}} = 10^3 \text{ cm}^{-3}$, grains larger than $a_{\text{align}} = 0.055 \mu\text{m}$ can be aligned by RATs. However, the radiation strength is not an observable quantity, thus we could use the dust temperature T_{d} as a proxy for this strength. If we adopt $U \approx (T_{\text{d}}/16.4 \text{ K})^6 (a/10^{-5} \text{ cm})^{6/15}$ (Draine, 2011), $a_{\text{align}} \sim n_{\text{H}}^{2/7} T_{\text{dust}}^{-12/7}$ that illustrates that higher T_{d} is able to bring smaller grains to align. Vice-versa, only larger grains are able to align in higher n_{H} (denser gas). Note that the power index in Eq. 32 slightly differs from Hoang et al. (2021b) and Tram et al. (2021b). The reason is due to the slightly difference in the scaling of the average RAT efficiency, but this difference results in a negligible discrepancy of a_{align} (see Figure 1 in Hoang et al., 2021b).

2.5.2.3 k-RAT vs. B-RAT Alignment

Using Eq. 31 one calculates the radiative precession (k-RAT) timescale for grains aligned at low- J attractors with $St = 1$ as

$$\tau_k^{\text{low-}J} = 56.4 \hat{\rho}^{1/2} T_1^{1/2} \hat{s}^{-1/6} a_{-5}^{1/2} \left(\frac{1.2 \mu\text{m}}{\gamma \bar{\lambda} \bar{Q}_{e3} U} \right) \text{yr}, \quad (33)$$

and for grains aligned at high- J attractors with $St = St_{\text{RAT}}$ from Eq. 14, one has

$$\tau_k^{\text{high-}J} = 1.17 \times 10^6 \hat{s}^{-1/3} \left(\frac{\hat{\rho} a_{-5}}{\hat{Q}_{e3}} \right) \left(\frac{1}{n_3 T_1^{1/2}} \right) \left(\frac{1}{1 + F_{\text{IR}}} \right) \text{yr}. \quad (34)$$

In the presence of a magnetic field, the grain experiences simultaneous Larmor precession and radiative precession. If the Larmor precession is faster than the radiative precession, i.e., $\tau_B < \tau_k$, the axis of grain alignment by RATs changes from with J along k to the magnetic field, B , which is known as B-RAT. The minimum grain size that grain alignment still occurs via k-RAT, which is also the maximum size grains can be aligned via B-RAT, is defined by $\tau_k = \tau_B$ and is derived in Hoang T. et al. (2022). For grains aligned at a low $-J$ attractor, one has

$$a_{\text{min,jk}}^{\text{low-}J,\text{PM}} \equiv a_{\text{max,jb}}^{\text{low-}J,\text{PM}} \approx 2.96 \hat{\rho}^{-1/2} \hat{s}^{-1/9} \left(\frac{\bar{\lambda}}{1.2 \mu\text{m}} \right)^{-2/3} \times \left(n_{23} f_p \frac{\hat{p}^2 T_1^{1/2}}{T_{d,1} \gamma U_3 \hat{Q}_{e3}} \right)^{2/3} \left(\frac{B}{20 \mu\text{G}} \right)^{2/3} \mu\text{m}, \quad (35)$$

and

$$a_{\text{min,jk}}^{\text{low-}J,\text{SPM}} \equiv a_{\text{max,jb}}^{\text{low-}J,\text{SPM}} = 57.8 \hat{\rho}^{-1/2} \hat{s}^{-1/9} \left(\frac{\bar{\lambda}}{1.2 \mu\text{m}} \right)^{-2/3} \times \left(\frac{\hat{p}^2 T_1^{1/2}}{T_{d,1} \gamma U_3 \hat{Q}_{e3}} \right)^{2/3} \times \left(\frac{B}{20 \mu\text{G}} \right)^{2/3} (N_{\text{cl},4} \phi_{sp,-2})^{2/3} \mu\text{m}. \quad (36)$$

for PM and SPM grains, respectively. The above equations imply that the minimum size for k-RAT when grains aligned at low $-J$ attractors is smaller for higher radiation strength as $U^{-2/3}$, but larger for stronger magnetic field as $B^{2/3}$. It is harder to bring SPM grains to align with the radiation direction because of their larger magnetic susceptibility and then faster Larmor precession.

Similarly, for grains aligned at a high $-J$ attractor (Hoang T. et al., 2022)

$$a_{\text{min,jk}}^{\text{high-}J,\text{PM}} \equiv a_{\text{max,jb}}^{\text{high-}J,\text{PM}} \approx 3.3 \times 10^8 \hat{s}^{-1/3} \left(\frac{n_{23} f_p \hat{p}^2}{n_3 T_{d,1} T_1^{1/2} \hat{Q}_{e3}} \right) \times \left(\frac{B}{20 \mu\text{G}} \right) \left(\frac{1}{1 + F_{\text{IR}}} \right) \mu\text{m}, \quad (37)$$

and

$$a_{\text{min,jk}}^{\text{high-}J,\text{SPM}} \equiv a_{\text{max,jb}}^{\text{high-}J,\text{SPM}} \approx 2.8 \times 10^{10} \hat{s}^{-1/3} \times \left(\frac{\hat{p}^2}{n_3 T_{d,1} T_1^{1/2} \hat{Q}_{e3}} \right) \left(\frac{B}{20 \mu\text{G}} \right) \times \left(\frac{N_{\text{cl},4} \phi_{sp,-2}}{1 + F_{\text{IR}}} \right) \mu\text{m}. \quad (38)$$

One realizes that the minimum size for k-RAT alignment is very large for typical molecular clouds, especially when grains are aligned at high- J attractors. Therefore, in these conditions, grains are aligned with J along the magnetic field via B-RAT. Yet, for very strong radiation fields of strength of $U \gg 1$, small grains at low- J attractors can have k-RAT alignment.

2.6 Radiative torque disruption (RAT-D)

2.6.1 The RAT-D mechanism

A dust grain rotating with an angular velocity Ω develops a tensile stress $S = \rho \Omega^2 a^2 / 4$ on grain material. This stress points outward from the grain center of mass and tends to tear the grain apart. When the tensile stress exceeds the maximum tensile strength of the grain material, S_{max} , the grain is instantaneously disrupted in fragments. The maximum angular velocity beyond which the grain is disrupted is defined by $S = S_{\text{max}}$ and reads

$$\Omega_{\text{disr}} = \frac{2}{a} \left(\frac{S_{\text{max}}}{\rho} \right)^{1/2} \approx \frac{3.65 \times 10^8}{a_{-5}} S_{\text{max},7}^{1/2} \hat{\rho}^{-1/2} \text{rads}^{-1}, \quad (39)$$

where $S_{\text{max},7} = S_{\text{max}} / (10^7 \text{erg cm}^{-3})$. The exact value of S_{max} depends on the grain internal structure (see Hoang, 2020, and references therein). For example, composite grains have $S_{\text{max}} \sim 10^7 \text{erg cm}^{-3}$, whereas compact grains have a higher value.

Subject to a strong radiation field, dust grains will be spontaneously fragmented into many smaller species when the grain angular velocity spun-up by RATs, Ω_{RAT} , exceeds the critical value Ω_{disr} . This is called the radiative torque disruption (RAT-D) mechanism, which was first introduced in Hoang et al. (2019). Due to the dependence of Ω_{RAT} on the grain size and local conditions, there is a range of grain sizes that can be disrupted, as illustrated by the shaded areas in Figure 3. The minimum size of grains that can be disrupted by RAT-D is

$$a_{\text{disr}} = \left(\frac{0.8 n_{\text{H}} \sqrt{2 \pi m_{\text{H}} k T_{\text{gas}}}}{\gamma u_{\text{rad}} \bar{\lambda}^{-2}} \right)^{1/2} \left(\frac{S_{\text{max}}}{\rho} \right)^{1/4} (1 + F_{\text{IR}})^{1/2} \approx 1.7 \left(\frac{\gamma_{-1} U}{n_3 T_1^{1/2}} \right)^{-1/2} \left(\frac{\bar{\lambda}}{1.2 \mu\text{m}} \right)^{\hat{\rho}^{-1/4}} S_{\text{max},7}^{1/4} \times (1 + F_{\text{IR}})^{1/2} \mu\text{m}, \quad (40)$$

and the maximum size of grains that can still be disrupted by RAT-D is as follows:

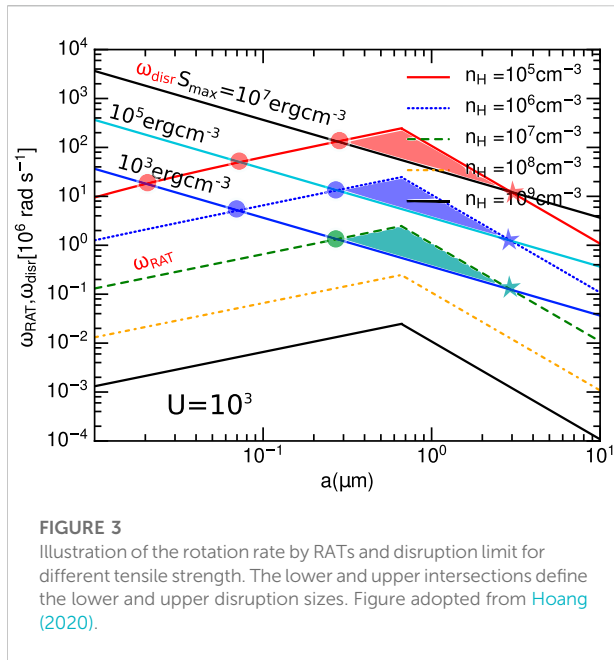
$$a_{\text{disr,max}} = \frac{\gamma u_{\text{rad}} \bar{\lambda}}{16 n_{\text{H}} \sqrt{2 \pi m_{\text{H}} k T_{\text{gas}}}} \left(\frac{S_{\text{max}}}{\rho} \right)^{-1/2} (1 + F_{\text{IR}})^{-1} \approx 0.03 \left(\frac{\gamma_{-1} U}{n_3 T_1^{1/2}} \right) \left(\frac{\bar{\lambda}}{1.2 \mu\text{m}} \right)^{\hat{\rho}^{1/2}} S_{\text{max},7}^{-1/2} \times (1 + F_{\text{IR}})^{-1} \mu\text{m}, \quad (41)$$

which depend on the local gas properties, radiation field, and the grain tensile strength (Hoang and Tram, 2020; Hoang et al., 2021b).

As shown, the RAT-D efficiency, described by the values of a_{disr} and $a_{\text{disr,max}}$, strongly depends on the local conditions, i.e., more efficient for higher radiation strength (U) or T_{d} , but less efficient for higher n_{H} .

2.6.2 Rotational desorption of ice mantles

Detection of interstellar complex organic molecules (COMs) are extensively reported toward low-/high-mass protostars and



protoplanetary disks (see e.g., van Dishoeck, 2014, and references therein). As a popular scenario, COMs are believed to first form on the icy mantle of dust grains (e.g., Garrod et al., 2008; Jiménez-Serra et al., 2016), and subsequently desorbed to the gas phase during the warm and hot phase, where icy grain mantles can be heated to high temperatures $T_d \sim 100 - 300$ K (see e.g., Blake et al., 1987; Brown et al., 1988; Bisschop et al., 2007). However, icy mantles might not be survived under an intense radiation field before the critical temperature for thermal sublimation is reached (Hoang and Tram, 2020). The centrifugal force can break the icy mantle from the bare core, then the evaporation and sublimation processes are enhanced owing to smaller size of the icy fragments, enabling COMs to release (see Figure 4A). This non-thermal process is called the rotational desorption, and found to be effective at lower dust temperatures than the classical thermal sublimation, which is able to explain the detection of COMs in cold regions (see Hoang and Tram, 2020; Tram et al., 2021c for further details).

Figure 4B shows an evidence for rotation desorption of COMs from Orion BN/KL region. The timescales of rotational desorption (color lines) and thermal sublimation (dashed dotted black lines) for three COMs with very high binding energy, including ethyl formate (C_2H_5OCHO), methoxymethanol (CH_3OCH_2OH) and ethylene glycol ($OHCH_2CH_2OH$) that are reported in Tercero et al. (2018), are shown for comparison. One can see that for given low dust temperatures constrained by SOFIA/FORCAST observations ($T_d \approx 80-100$ K; De Buizer et al., 2012), rotational desorption is more effective than thermal sublimation in desorbing COMs from the grain surface. With regard to the UV photo-desorption (dashed horizontal lines), the rotational desorption could be as efficient as (or more effective

than) the UV photo-desorption regarding to the photo-desorption yield uncertainty. However, UV photons are expected to be quickly attenuated by dust absorption, so that the volume in which photo-desorption is important is less extended than the rotational desorption which can work with optical-IR photons.

2.7 Summary of grain alignment and disruption in molecular clouds

In this section, we discuss the alignment of magnetic grains in a typical molecular cloud, which is irradiated by an ionization source (e.g., OB stars). We adopted the following representative parameters: $n_H = 10^3 \text{ cm}^{-3}$, $T_{\text{gas}} = T_d = 30$ K, $U \approx a_{-5}^{6/15} (T_d/16.4 \text{ K})^6$, $\bar{\lambda} = 0.5 \mu\text{m}$, $\gamma = 1.0$, and $B = 20 \mu\text{G}$. The maximum grain size is limited to $100 \mu\text{m}$.

Figure 5A illustrates the relative importance of different alignment mechanisms. For the internal alignment, most grains are aligned with the angular momentum parallel to the short axis (i.e., $\mathbf{J} \parallel \mathbf{a}_1$). The paramagnetic relaxation is much less efficient than the Larmor precession. Grains can be aligned by RATs along B-fields (B-RAT) up to sizes of $1.1 \mu\text{m}$. Above that size, the radiative precession is faster than the Larmor precession such that grains are turned to align with the radiation direction (k-RAT). Hence, B-RAT is the most important alignment mechanism in the diffuse ISM and typical molecular clouds where dust grains could not grow to beyond $1 \mu\text{m}$. Furthermore, if the grain's structure is not very compact (e.g., with a low tensile strength of $S_{\text{max}} = 10^8 \text{ erg cm}^{-3}$), the RAT-D mechanism can disrupt large grains with size of $0.1-7.5 \mu\text{m}$. The rotational fragmentation enhances the abundance of smaller grains, which, in turn, can allow more grains to align with the magnetic field.

Similarly, Figure 5B shows alignment for superparamagnetic grains with $N_{cl} = 10^3$ and $\phi_{sp} = 0.01$. Due to the enhancement of susceptibility, all superparamagnetic grains are aligned with $\mathbf{J} \parallel \mathbf{a}_1$ for the internal alignment. For the external alignment, B-RAT alignment is dominant over k-RAT. Even the DG mechanism is more effective for larger grains up to $6.5 \mu\text{m}$ compared to ordinary paramagnetic grains, yet the B-RAT is much more efficient than the superparamagnetic relaxation. Thus, superparamagnetic grains are precessed along the external magnetic fields.

Therefore, grain alignment is able to probe the magnetic field in typical molecular clouds. However, as shown in this section, the gas damping, the B-field strength and the radiation strength are as key to characterize which alignments take place. Hence, all of alignment sizes are subjected to change with the local conditions, and the picture of grain alignment become very complicated in very dense regions, such as protostellar cores/disks (see Section 5.2).

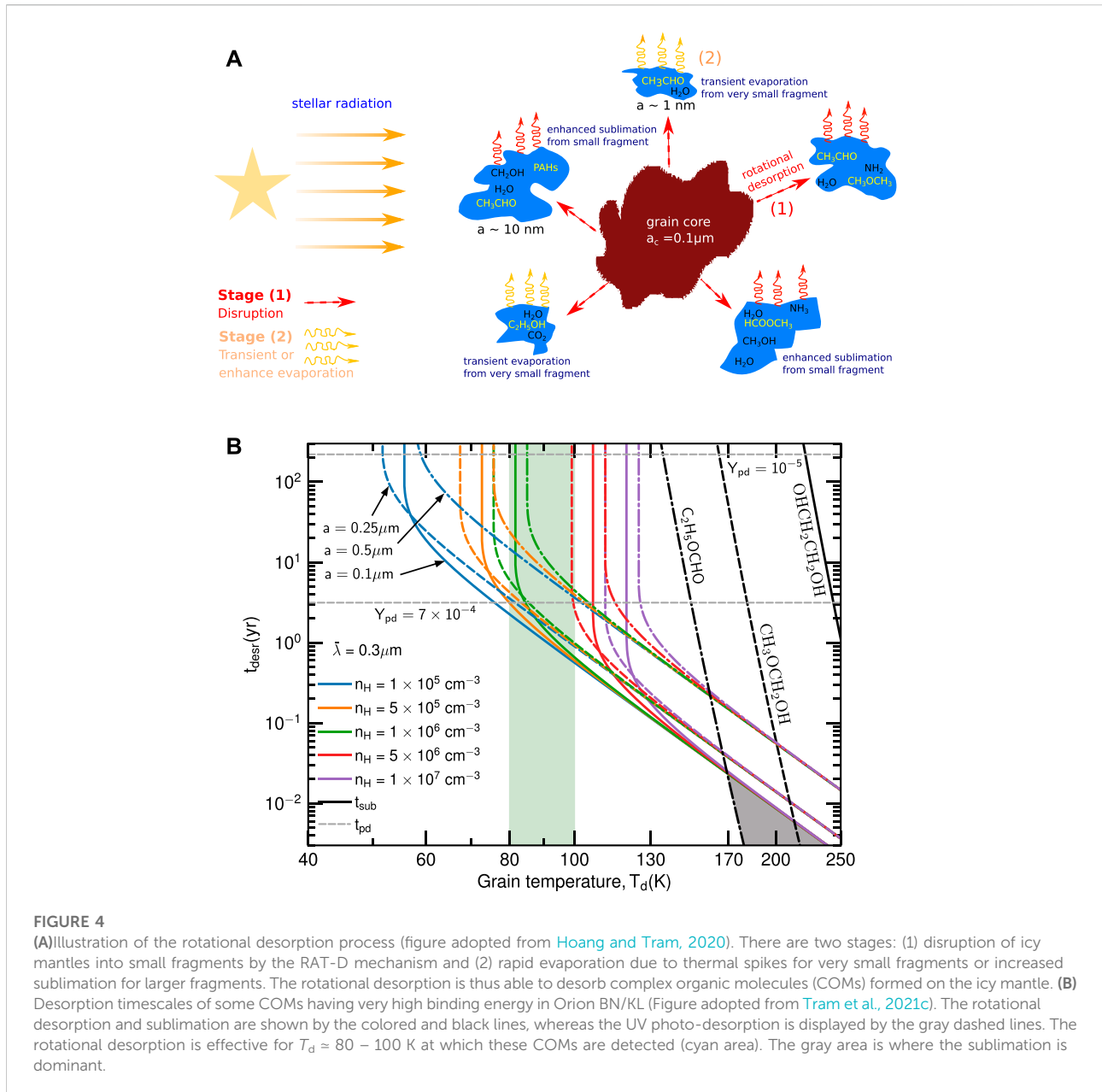


FIGURE 4 (A) Illustration of the rotational desorption process (figure adopted from Hoang and Tram, 2020). There are two stages: (1) disruption of icy mantles into small fragments by the RAT-D mechanism and (2) rapid evaporation due to thermal spikes for very small fragments or increased sublimation for larger fragments. The rotational desorption is thus able to desorb complex organic molecules (COMs) formed on the icy mantle. (B) Desorption timescales of some COMs having very high binding energy in Orion BN/KL (Figure adopted from Tram et al., 2021c). The rotational desorption and sublimation are shown by the colored and black lines, whereas the UV photo-desorption is displayed by the gray dashed lines. The rotational desorption is effective for $T_d = 80 - 100$ K at which these COMs are detected (cyan area). The gray area is where the sublimation is dominant.

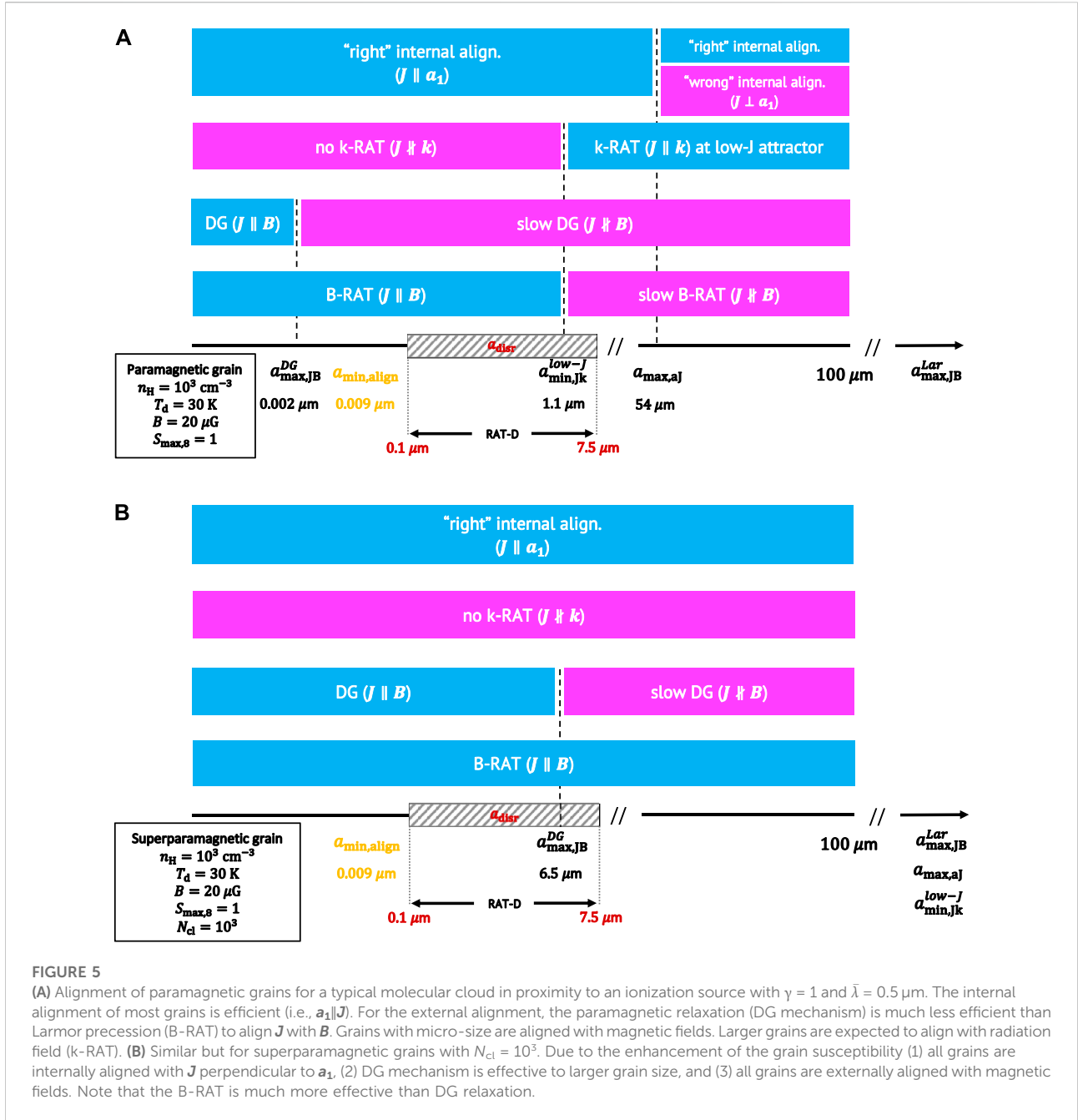
3 Modeling thermal dust polarization within the RAT paradigm

Polarized thermal dust emission depends on the grain properties (size, shape, and composition), grain alignment degree, and the magnetic field geometry (see e.g., Draine and Fraisse, 2009). Within the RAT paradigm, RATs can induce the simultaneous effects of RAT-A and RAT-D on dust grains. The RAT-A describes the alignment degree of grains of different sizes with the magnetic field, whereas RAT-D affects the grain size distribution. Therefore, an accurate physical model of polarized thermal dust emission requires the treatment of both RAT-A and RAT-D effects.

3.1 Assumptions and basic equations

To account for both the RAT-A and RAT-D effects on dust polarization, Lee et al. (2020) adopted a simple cloud model⁴ consisting of a homogeneous molecular cloud irradiated by a central radiation source, as illustrated in Figure 6A. The radiation strength (U) decreases with distance from the central star and varies along the line of sight (solid and dashed lines). For simplicity, all

⁴ The state-of-the-art version is publicly available at <https://github.com/lengoctram/DustPOL>



grains along each line of sight in the cloud are assumed to be illuminated by the constant radiation field of strength U .

As shown in Section 2.4 (also Section 2.7), both Barnett and inelastic relaxation effects are very efficient for standard grains in the ISM and MCs, leading to the perfect internal alignment of dust grains (see Figure 5). Therefore, grain alignment is mostly determined by external alignment by RATs. For the rotational damping, we consider only collisions with gas and re-emission of thermal dust as two main sources to damp the grain rotation against the spin-up by RATs. The variation of B-fields along the line of sight is neglected by assuming the uniform magnetic field (the field tangling effect is discussed in

Section 4.5). The detailed description of this model was presented in Lee et al. (2020) and Tram et al. (2021a).

Dust grains are heated by absorption of the stellar radiation and cool down by re-emission in infrared radiation. Assuming a dust environment containing carbonaceous and silicate grains, the total dust emission intensity is given by

$$\frac{I_{\text{em}}(\lambda)}{N_H} = \sum_{j=\text{sil,carb}} \int_{a_{\text{min}}}^{a_{\text{max}}} Q_{\text{ext}}(a, \lambda) \pi a^2 \times \int dTB_\lambda(T_d) \frac{dP}{dT} \frac{1}{n_H} \frac{dn_j}{da} da. \quad (42)$$

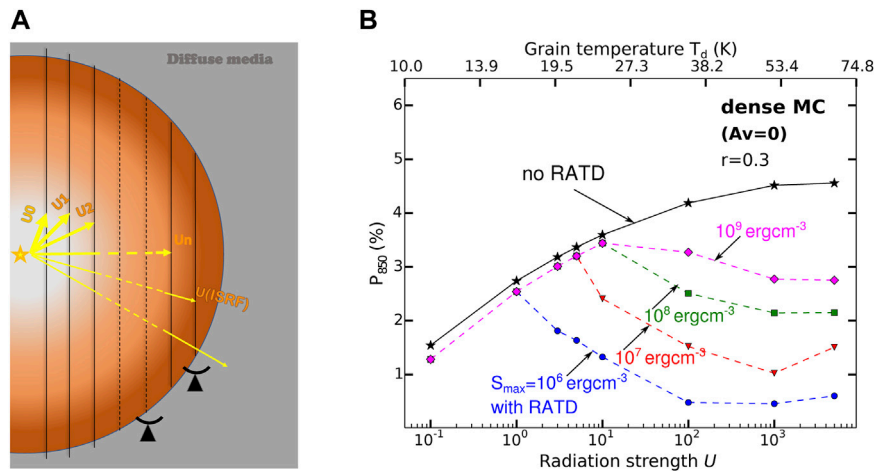


FIGURE 6

(A) Schematic illustration of the model. A molecular cloud is irradiated by the central star, so that the radiation strength decreases from U_0 to U_{ISRF} . The color gradient indicates the increase of the gas density from the central star. Magnetic fields are assumed to be uniform. (B) An example of polarization degree vs. radiation strength (dust temperature) at $850 \mu\text{m}$ predicted by the numerical model (Lee et al., 2020). If we consider only the RAT-A effect, the polarization degree monotonically increases with increasing the radiation strength (dust temperature) as expected (black line). If we take into account the RAT-D mechanism, rotational disruption occurs when the radiation strength (dust temperature) is sufficiently high. Once this happens, the depletion of largest grains results in the decrease of the polarization degree (color lines). Figure taken from Lee et al. (2020) and Tram et al. (2021a).

where a_{min} and a_{max} are the minimum and maximum grain sizes, N_{H} is the hydrogen column density, $B_{\lambda}(T_{\text{d}})$ is the Planck function at dust temperature T_{d} , dP/dT is the grain temperature distribution function, dn_j/da is the grain-size distribution of dust population j , and Q_{ext} is the extinction coefficient. The dust temperature distribution depends on the grain size, optical constant, and the radiation field (U), which is computed by the DustEM code (Compiègne et al., 2011, see e.g., Figure 8 in Lee et al., 2020).

If silicate and carbon dust populations are separated, then as paramagnetic grains, silicates can align with the ambient magnetic field, whereas carbonaceous grains cannot. Thus, the polarized emission intensity resulting from aligned grains is given by (Hoang and Lazarian, 2016a)

$$\frac{I_{\text{pol}}(\lambda)}{N_{\text{H}}} = \int_{a_{\text{min}}}^{a_{\text{max}}} f(a) Q_{\text{pol}} \pi a^2 \times \int dTB_{\lambda}(T_{\text{d}}) \frac{dP}{dT} \frac{1}{n_{\text{H}}} \frac{dn_{\text{sil}}}{da} da, \quad (43)$$

where $f(a) = 1 - \exp[-(a/2a_{\text{align}})^3]$ is the alignment function, and Q_{pol} is the polarization efficiency coefficient.

If silicate and carbon grains are mixed together (e.g., Jones et al., 2013; Draine and Hensley, 2021), which may be the case in dense clouds due to many cycles of photo-processing, coagulation, shattering, accretion, and erosion, carbon grains could be aligned with the ambient magnetic field and their thermal emission could be polarized. In the simplest case, assuming these grain populations have the same alignment

parameters (i.e., a_{align} and $f(a)$), the total polarized intensity is as follows:

$$\frac{I_{\text{pol}}(\lambda)}{N_{\text{H}}} = \sum_{j=\text{sil,carb}} \int_{a_{\text{min}}}^{a_{\text{max}}} f(a) Q_{\text{pol}} \pi a^2 \times \int dTB_{\lambda}(T_{\text{d}}) \frac{dP}{dT} \frac{1}{n_{\text{H}}} \frac{dn_j}{da} da. \quad (44)$$

The extinction (Q_{ext}) and polarization coefficients (Q_{pol}) are computed by the DDSCAT model (Draine and Flatau, 1994, 2008; Flatau and Draine, 2012). The maximum grain size is constrained by the RAT-D mechanism, $a_{\text{max}} \equiv a_{\text{disr}}$.

The fractional polarization of the thermal dust emission is the ratio of the polarized intensity (I_{pol}) to the total emission intensity (I_{em}), which yields the following:

$$P(\%) = 100 \times \frac{I_{\text{pol}}}{I_{\text{em}}}. \quad (45)$$

3.2 Model parameters and numerical prediction

Our model parameters include the gas properties (gas number density, n_{H}) and gas temperature, T_{gas}), the dust properties (size a , shape, internal structure described by the tensile strength S_{max} , and size distribution power index β),

and the ambient properties (radiation field strength U , mean wavelength $\bar{\lambda}$, and an anisotropy degree γ of the radiation field).

Radiation strength cannot be constrained from observations, thus, the equilibrium temperature of dust grains is used as a proxy of the radiation strength, as $U \approx a_{-5}^{6/15} (T_d/16.4 \text{ K})^6$. Here, the dust temperature is derived from fitting a modified black-body function to the continuum spectral energy distribution. The mean wavelength ($\bar{\lambda}$) of the stellar radiation field from a central source with T_* is given as $\bar{\lambda} \approx 0.53 \text{ cm K}/T_*$ (see Eq. 8 in Hoang et al., 2021b). The internal structure of grains is determined via their tensile strength (S_{max}). Unfortunately, this quantity is poorly constrained in astrophysical environments. However, compact grains in general are expected to have higher S_{max} than composite and fluffy grains. For instance, one expects $S_{\text{max}} \sim 10^9\text{--}10^{10} \text{ erg cm}^{-3}$ for compact grains, whereas $S_{\text{max}} \sim 10^6\text{--}10^8 \text{ erg cm}^{-3}$ for composite grains (see e.g., Hoang, 2020). In the model, S_{max} can be set as a free parameter.

Figure 6B shows the predicted dependence of the polarization degree on radiation strength (or dust temperature) at a specific wavelength of $850 \mu\text{m}$ for $n_{\text{H}} = 10^4 \text{ cm}^{-3}$. In the case of only RAT-A effect (black line), the polarization degree increases as radiation strength (dust temperature) increases. In the case of both RAT-A and RAT-D effects, the polarization degree first increases and turns to decrease toward higher dust temperature. The second trend is caused by the rotational disruption which occurs above a critical temperature. For dust temperatures lower than the critical temperature, RATs are not enough to spin-up grains to the disruption limit Ω_{disr} , so that the RAT-D cannot occur. Thus, the results are the same as in the case of only RAT-A effect. For dust temperatures higher than the critical value, RATs become stronger to trigger the RAT-D effect, resulting in rotational disruption of large grains into small fragments. This leads to a drop in the polarization degree due to the depletion of large grains. This critical temperature and the level of the decline depend on the internal structure of the grains controlled by S_{max} .

Figure 7 shows our understanding of the trend of polarization degree versus radiation strength/dust temperature shown in Figure 6B. For a given gas density, the polarization degree is mainly determined by the grain size distribution. If the only RAT-A effect is considered, the maximum grain size is fixed. The minimum size that is aligned by RATs is smaller for higher radiation strength (more small grains are able to be aligned). Hence, the size distribution of aligned grains becomes broader, which deduces the increment of the polarization degree. If the rotational disruption is taken into account along with the RAT-A effect, the maximum grain size could vary. In this case, if the radiation is insufficient strong the polarization degree is observed to increase with radiation strength as previous case. Once the radiation strength is sufficient to trigger disruption, the maximum grain size reduces from a_{max} to a_{disr} . The narrower size distribution of aligned grains causes the polarization degree to drop.

As we mentioned, radiation strength is not an observable quantity, thus dust temperature could be used as a proxy. Therefore, the relation between polarization degree and dust temperature ($p - T_d$) becomes a unique tool to study the joint effect of grain alignment and disruption by RATs.

4 Observational study of the RAT effects in star-forming regions

In this section, we review our observational results of thermal dust polarization observed toward star-forming molecular clouds, including ρ Ophiuchus-A, 30 Doradus, M 17, and Orion BN/KL. These star-forming MCs containing intense radiation sources are the ideal targets to test the RAT-A and RAT-D effects.

4.1 ρ Ophiuchus-A

ρ Ophiuchus-A (ρ Oph-A) is a molecular cloud in one of the closest dark cloud complex and star-forming region ρ Ophiuchi. The distance to this complex is reported to be $\sim 120\text{--}160 \text{ pc}$ (Chini, 1981; de Geus et al., 1989; Ortiz-León et al., 2017). This cloud is irradiated by a high-mass star, namely Oph-S1, which is a young B3-type star (Vrba 1977; Hamaguchi et al., 2003).

Figure 8 shows the observational data of ρ Oph-A. The top panels show the maps of gas column density (panel (a)) and dust temperature (panel (b)) constructed from *Herschel*. Along the radial direction toward Oph-S1 (marked by the white star), the dust is hotter while the gas is more diffuse. The middle and bottom panels show the $p - T_d$ relations. Background shows the observational data at $89 \mu\text{m}$ (left) and $154 \mu\text{m}$ (right) observed by SOFIA/HAWC+. The polarization degree tends to first increase and then decrease as the dust temperature increases. One can see that the latter decrement occurs in vicinity of Oph-S1 where the gas density is lower. Therefore, the drop of p toward higher T_d and lower n_{H} is opposite to the fundamental prediction of the RAT-A effect.

The lines in Figure 8 show the results from our numerical modeling overplotted with the observational data at two wavelengths, assuming only silicate (panels (c,d)) or a combination of silicate and carbonaceous grains (panels (e,f)) with different slopes (β) of the size distribution. We considered two cases: only the RAT-A effect (no RAT-D, dashed line) and both RAT-A and RAT-D effects (solid lines).

- For the former case, the polarization degree monotonically increases with the dust temperature. This rising $p - T_d$ trend is caused by the increase in the alignment efficiency (i.e., decrease in the alignment size a_{align}) toward the Oph-S1 due to stronger radiation intensity and lower gas density. Obviously, the RAT-A effect is able to

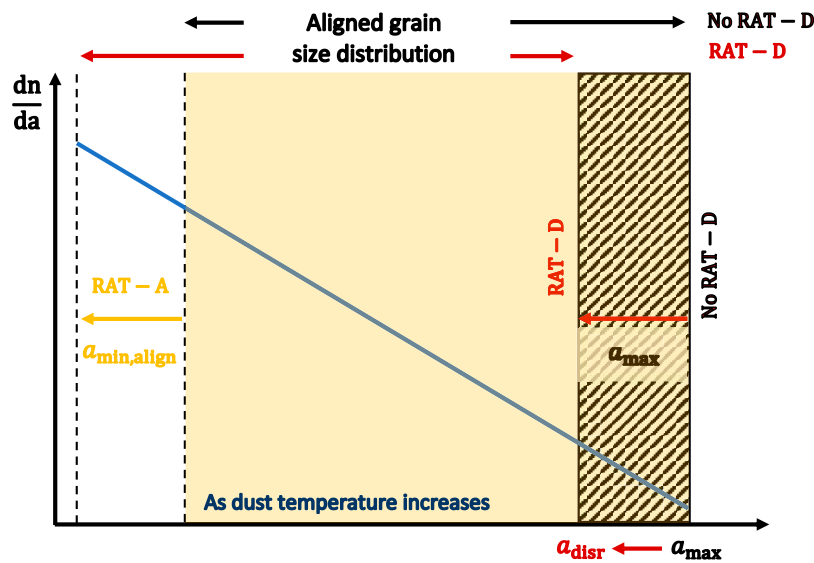


FIGURE 7

Understanding of thermal dust polarization. For a fixed maximum grain size (a_{\max}), higher radiation strength/dust temperature can bring smaller grains to align (smaller size of $a_{\min,\text{align}}$) so that the aligned grain size distribution becomes broader. This broad size distribution increases the degree of thermal dust polarization with radiation strength/dust temperature. If the maximum grain size is determined by the RAT-D mechanism and grains are composite ($a_{\max} \rightarrow a_{\text{disr}}$), higher radiation/dust temperature results in smaller a_{disr} . The consequent narrower aligned grain size distribution drops the polarization degree.

reproduce the first increasing part of the observational data, but not the second decreasing part.

- For the latter case, the polarization degree is similarly expected to increase for $T_d \approx 34$ K. At higher dust temperatures, the RAT-D happens for grains larger than a_{disr} owing to the higher radiation intensity and the lower gas density, which reduces the polarization degree. The joint effect of RAT-A and RAT-D mechanisms is therefore able to reproduce the entire observational data.

4.2 30 Doradus

30 Doradus (30 Dor), the Tarantula Nebula, is an HII region located in the Large Magellanic Cloud (LMC) at the distance of ~ 50 kpc from the Sun (e.g., De Marchi et al., 2011). It is powered by the massive star cluster R 136 that has a bolometric luminosity of $7.8 \times 10^7 L_\odot$ (see Lopez et al., 2011, and references therein). Since the LMC is a low-metallicity galaxy ($Z \approx 0.5Z_\odot$, see e.g., Dufour et al., 1982; Galliano et al., 2008) that has a low dust-to-gas ratio (e.g., $\sim 2 - 5 \times 10^{-3}$; see Roman-Duval et al., 2014), the radiative feedback could be effective deeper inside the surrounding molecular cloud. Thus, the 30 Dor cloud offers a valuable environment to test the physics of grain alignment and disruption by RATs.

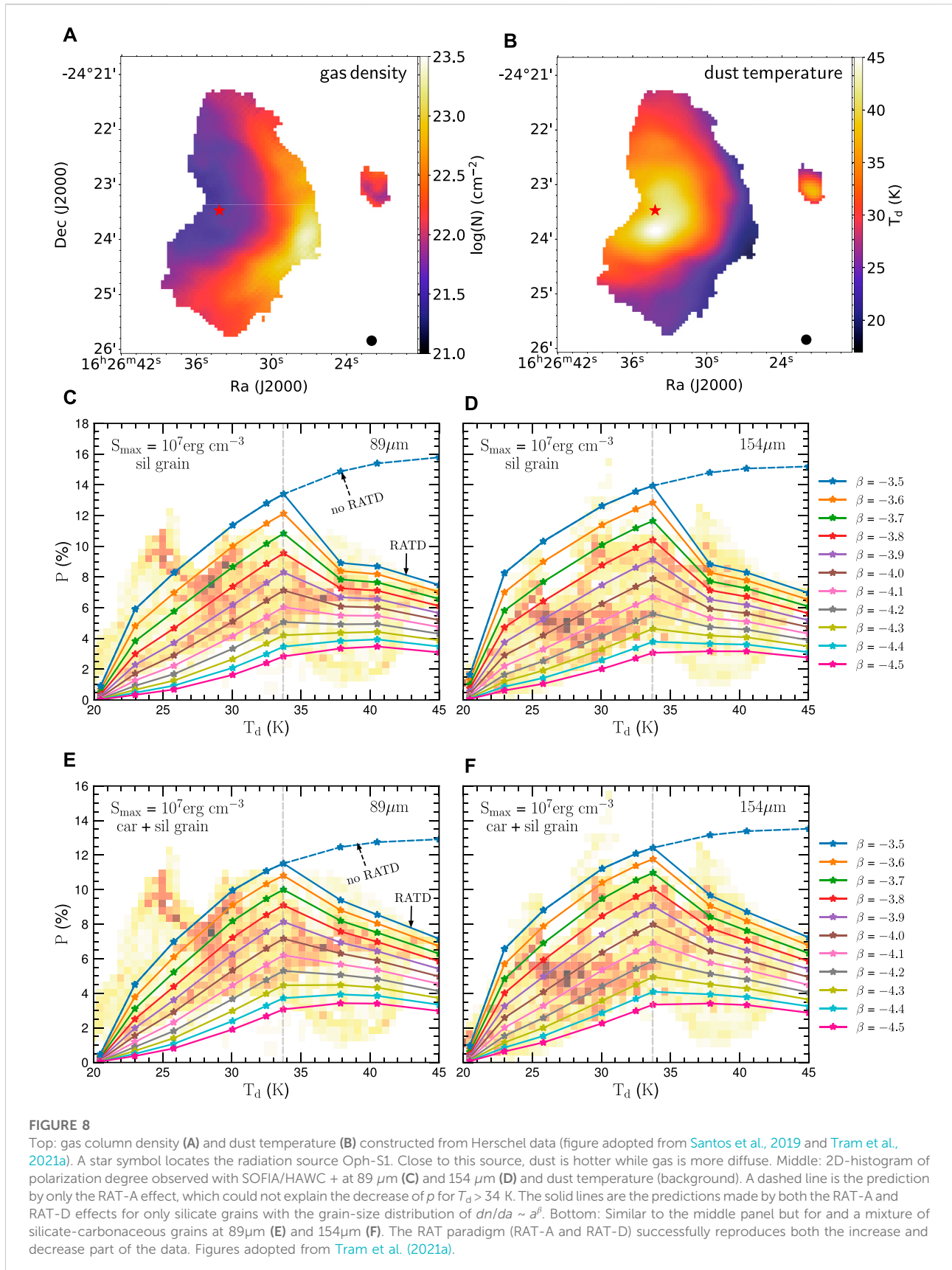
Figure 9A shows the polarization degree map observed with SOFIA/HAWC+ at $214 \mu\text{m}$. The location of ionization source R

136 is denoted by a red cross. For comparison, the contours show the map of gas column density. For further analysis, we selected two sub-regions, namely, north and south as highlighted respectively by a red box and a red ellipse. Figures 9B,C show the relation of the gas column density to the dust temperature in these two sub-regions, respectively. In the north, the gas density unambiguously increases and then decreases with increasing dust temperature. The transition is at $T_d \sim 37-40$ K. In the south, the relation is less clear. Yet, it is likely to behave similarly as in the north, in which the gas density positively correlates with the dust temperature up to $T_d \sim 37-39$ K, and negatively correlates with higher T_d .

Figure 10 shows the $p - T_d$ relations in the north (left panel) and in the south (right panel) for three SOFIA/HAWC+ wavelengths (from top to bottom).

1 In the north, there is a complex relation for all wavelength. Note that T_d increases toward R 136.

- For $T_d \leq 37 - 40$ K (region A), both dust temperature and gas column density increase. The polarization degree first rapidly drops, then rises, and finally slowly changes with increasing dust temperature. This trend could be explained by the RAT-A effect. Increasing gas density causes increased rotational damping by gas collisions, which is sufficiently efficient for larger a_{align} . As we discussed in Section 3, a higher value of a_{align} causes p to decrease. At some point in the cloud where T_d is sufficient high, the variation of a_{align} might be small because



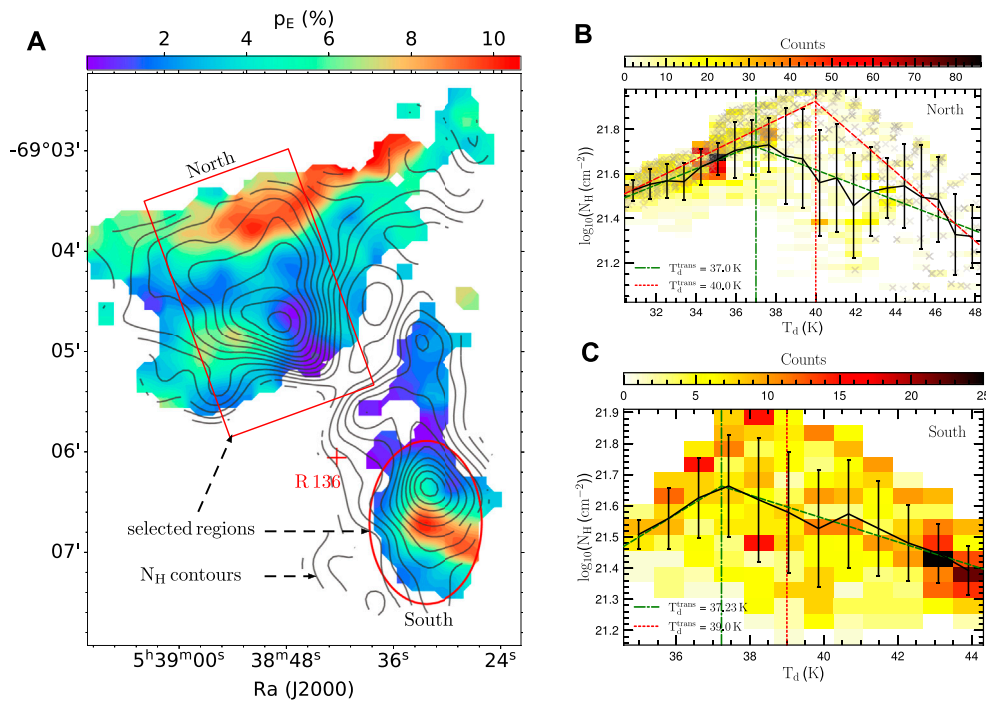


FIGURE 9

(A) SOFIA/HAWC + observations of 30 Dor at $214 \mu\text{m}$. Contours are the map of gas column density. The stellar cluster R 136 is located by a red cross. We selected two sub-regions, namely, north and south, to further analysis. (B,C) 2D-histogram of gas column density vs. dust temperature in two selected sub-regions: north and south. The black line shows the weighted mean in each bin associated with $1 - \sigma$ uncertainty. The blue line is a double power-law fitting. In the north, we fit to an upper envelope of the distribution by a dashed red line. In the south, the plot is more scatter. However, these quantities are positively correlated upto $T_d \approx 37 \text{ K}$ and negatively correlated to higher T_d . Figure adopted from Tram et al., 2021b.

of opposite effects of T_d and N_H . That makes p to slowly change.

- For $T_d > 37 - 40 \text{ K}$, the gas column density decreases, the polarization degree first increases slightly (regions B) and then drops again (region C). The negative slopes are steeper for longer wavelengths, namely -0.52 , -0.72 and -0.83 at 89, 154 and $214 \mu\text{m}$, respectively. As gas damping become less effective due to lower N_H and higher T_d , the RAT-A effect could explain the increase in p in region B (i.e., smaller a_{align}), but fails to explain the drop of p in region C. The latter is evidence for the RAT-D mechanism at work in proximity to radiation source where N_H continues to be small while T_d is highest. As the largest grains get disrupted, p decreases faster at longer wavelength. Thus, the observed drops of p in region C are expected by RAT-A and RAT-D.

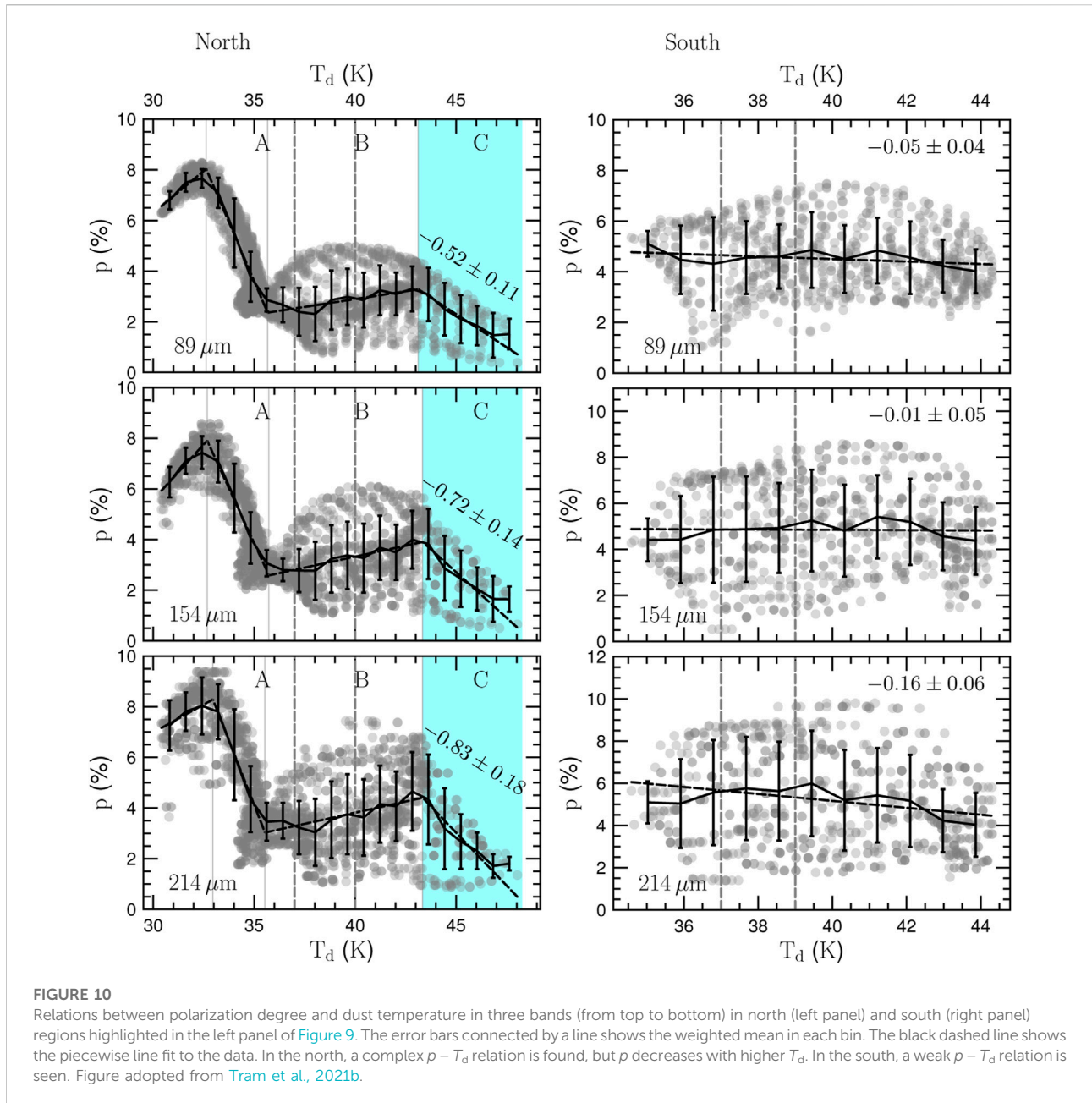
2 In the south, the $p - T_d$ relation has a high degree of scatter and is ambiguous. There might be three reasons for the slow variation of p with T_d . First, the saturation of RAT-D, which occurs at very high temperatures (i.e., T_d is much larger than the disruption threshold temperature; see Figure 14 in Lee et al., 2020). Small grains resulting from the disruption do not experience RAT-D due to lower RATs. Second, when dust grains are very hot, IR damping is so strong and dominates the gas damping, resulting

in the slow variation of a_{disr} with T_d . Third, effective gas damping due to the high gas density in the selected region (see Figure 9).

4.3 M17

M17, also known as the Omega Nebula or the Horseshoe Nebula is prominent HII region with and associated molecular cloud and star-forming region (Povich et al., 2009; Lim et al., 2020). It is located in the constellation of Sagittarius at a distance of 1.98 kpc (Xu et al., 2011). M17 hosts the stellar cluster NGC 6618 and its relative closeness makes it an excellent target to test the RAT paradigm.

Figure 11A shows the SOFIA/HAWC + observations of M17. Generally, the stellar cluster NGC 6618 (the most massive stars in this cluster are indicated by the white star symbols) are responsible for ionizing and creating the HII region. We divided M17 into two sub-regions, namely M17-N and M17-S. M17-S contains several compact sources as marked by white crosses. Figures 11B,C respectively show the relation between gas column density and dust temperature, and the relation of polarization degree with dust temperature. Lower density gas is associated with higher dust temperature.

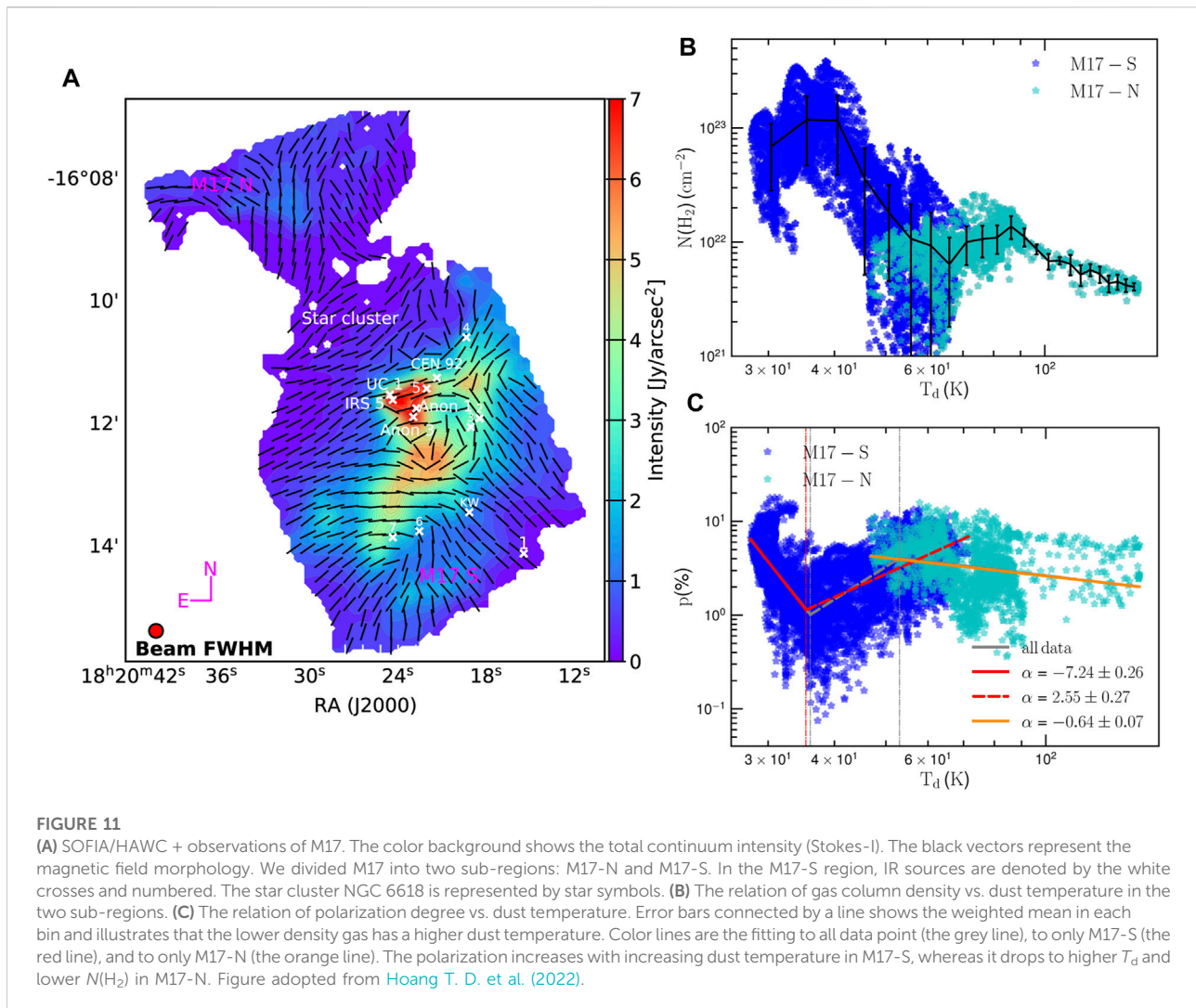


- In M17-S, where the density is relatively high, and the dust temperature is relatively low, the observed polarization degree increases with increasing dust temperature. In this condition of high gas density and low temperatures, gas damping is more efficient so that RAT-D cannot occur. Therefore, the increase of $p - T_d$ is consistent with the prediction of the RAT-A effect.
- In M17-N, where the gas density is rather low and the dust temperature is relatively high ($T_d \geq 60$ K), the observed polarization tends to decrease with T_d . In this condition of lower densities and high temperatures, RAT-D can easily

occur due to weak gas damping and strong RATs. As a result, the decrease in p with increasing T_d is consistent with the joint effect of RAT-A and RAT-D.

4.4 OMC-1 or Orion BN/KL

At a distance of ≈ 400 pc (Menten et al., 2007; Kounkel et al., 2017), the Orion nebula is the closest and the most extensive studied region of massive star-forming region. Due to its proximity, the arcsecond resolution observations of polarized



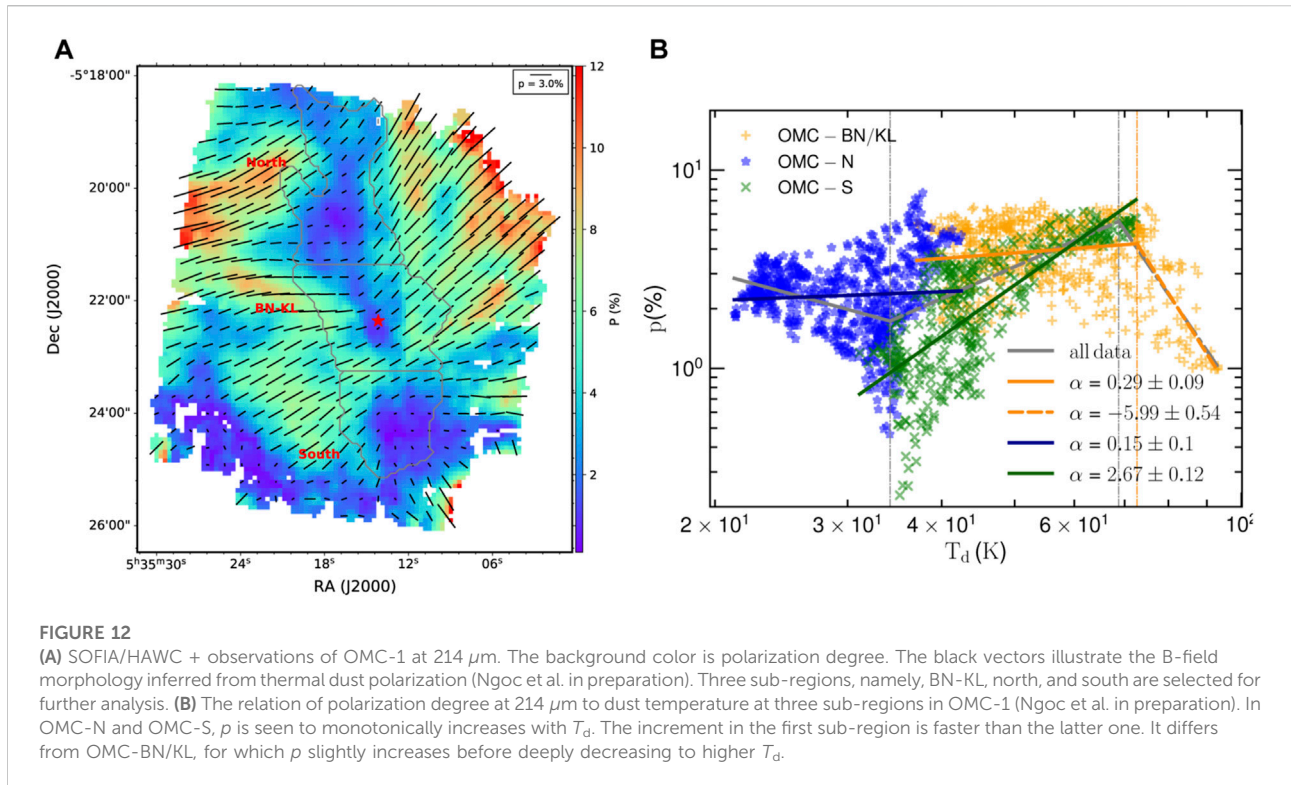
thermal dust that have been carried out sample scales of a few thousand AU (Pattle et al., 2017; Chuss et al., 2019; Ajeddig et al., 2022). These observations have provided a wealth of information of dust physics in the different physical environments of the Orion region. Here we focus on only OMC-1 region. This region can be divided into: 1) the Becklin–Neugebauer–Kleinmann–Low Nebula (BN/KL; Becklin and Neugebauer, 1967; Kleinmann and Low, 1967) which hosts on-going star formation; 2) the Southern clump (OMC-S; Batria et al., 1983) that is quiescent. These sub-regions are labeled in Figure 12A. We concentrated on the variation of the polarization degree along the main filament in Orion, in which we selected one more sub-region (OMC-N) north of BN/KL.

Figure 12B shows the variation of the polarization degree with the dust temperature for these three sub-regions. In two quiescent OMC-N and OMC-S, p increases with increasing T_d , which is predicted by the RAT-A effect. Since T_d is higher in

OMC-S, the grain alignment is more efficient resulting in more significant increment in this region compared to OMC-N, which is understandable in the RAT-A framework. However, the $p - T_d$ relation in OMC-BN/KL is different from other regions. The polarization degree slightly increases and then decreases for $T_d \geq 70$ K. At such high T_d , the rotational disruption is effective, leading to the decline of p . The RAT paradigm is therefore able to reproduce the $p - T_d$ relations in these three regions of OMC-1.

4.5 Can the anti-correlation of p vs. T_d arise from B-field tangling?

We showed that the anti-correlation of p vs. T_d is produced by RAT-D mechanism, assuming uniform magnetic fields. This disregard of the magnetic field tangling on variation of p could lead to biased conclusions. To check whether or not the field tangling could cause the decrease of p , we analyze the variation of



the polarization angle dispersion function S as a function of T_d . The biased dispersion at position \mathbf{r} on the sight-line is given as follows:

$$S_{\text{biased}}(\mathbf{r}) = \sqrt{\frac{1}{N} \sum_{i=1}^N [\psi(\mathbf{r} + \delta_i) - \psi(\mathbf{r})]^2} \quad (46)$$

where $\psi(\mathbf{r})$ and $\psi(\mathbf{r} + \delta)$ are the polarization angles at position \mathbf{r} and $\mathbf{r} + \delta$, respectively. In practice, for a given position \mathbf{r} we select all data points (N) within a circular aperture centered at this position with a diameter of two beam sizes.

Then the unbiased dispersion function is as follows:

$$S(\mathbf{r}) = \sqrt{S_{\text{biased}}^2(\mathbf{r}) - \sigma_s^2(\mathbf{r})} \quad (47)$$

whose an associated error is (see Eq. 8 in Planck Collaboration et al., 2020)

$$\sigma_s^2(\mathbf{r}) = \frac{1}{N^2 S^2} \sum_{i=1}^N \sigma_\psi^2(\mathbf{r} + \delta_i) [\psi(\mathbf{r} + \delta_i) - \psi(\mathbf{r})]^2 + \frac{\sigma_\psi^2(\mathbf{r})}{N^2 S^2} \left[\sum_{i=1}^N \psi(\mathbf{r} + \delta_i) - \psi(\mathbf{r}) \right]^2 \quad (48)$$

with $\sigma(\mathbf{r})$ and $\sigma(\mathbf{r} + \delta)$ the errors of polarization angle at the position \mathbf{r} and $\mathbf{r} + \delta$.

Figure 13 shows the variation of the dispersion angle S with T_d in 30 Dor (panel (a)) and in M17 (panel (b)). For 30 Dor, S is poorly correlated with T_d , indicating that the field tangling could

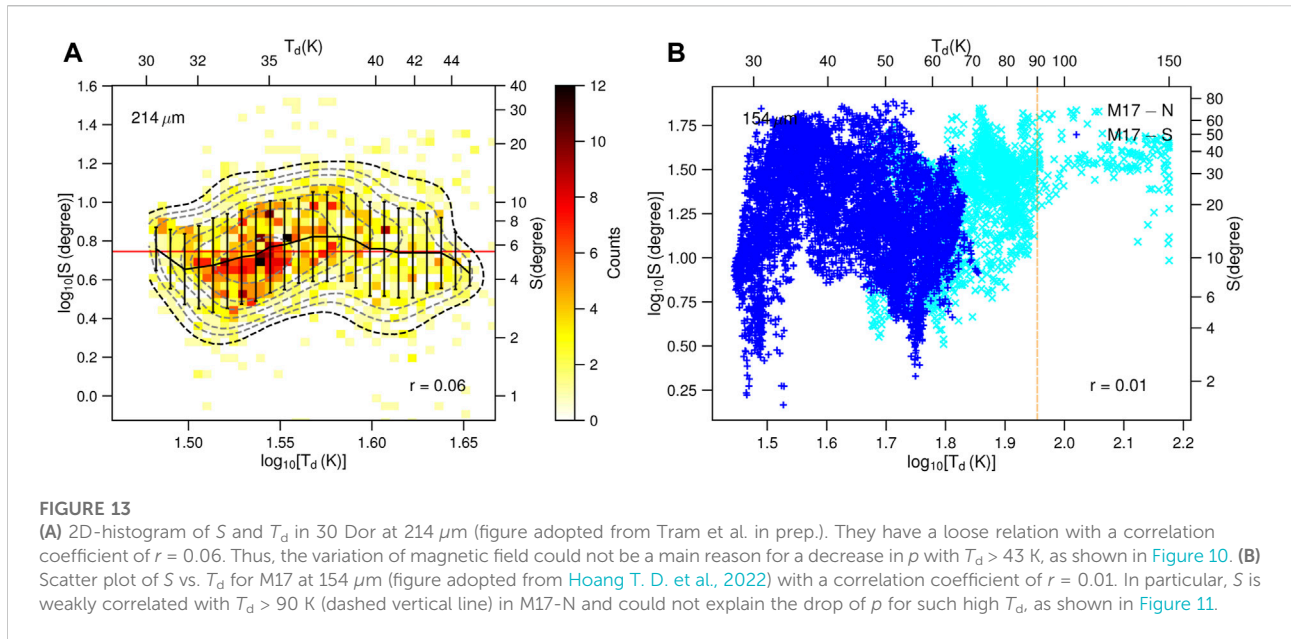
not be the main explanation for the anti-correlation of p vs. T_d as shown in Figure 10. In the case of M17, S slowly varies for $T_d > 90$ K. Similarly, the variation of the magnetic field ambiguously results in the $p - T_d$ relation in Figure 11). Via these two examples, one can see that the disruption of large grains in the vicinity of an intense radiation source is the major responsible for the decrease in p , instead of owing to the loss of alignment efficiency by gas collision and magnetic field tangling.

5 Discussion

5.1 Dust polarization as a reliable tracer of magnetic fields in star-forming regions

Magnetic fields are thought to play an important role in the evolution of the ISM and star formation. However, measurement of interstellar magnetic fields is rather difficult. One of the leading applications of dust polarization is tracing magnetic fields. Thus, the question of to what extent dust polarization can reliably trace the magnetic field is crucially important.

As reviewed in Section 2, grain alignment in the ISM and MCs is dominated by the RAT mechanism. The (super) paramagnetic material (e.g., silicate grains) is magnetized through the Barnett effect, which causes the grain to have rapid Larmor precession around the magnetic field. Moreover, Barnett and inelastic relaxation effects induce efficient internal



alignment of grain shortest axis with the angular momentum. The external alignment of the grain angular momentum along the ambient magnetic fields is dominated by B -RAT alignment because the Larmor precession is much faster than the gas randomization as well as the radiative precession. Thus, grains are aligned with their longest axes perpendicular to the magnetic field. The polarization orientation of thermal dust emission is perpendicular to, whereas the polarization of starlight by dust extinction is parallel to the local magnetic field. As a result, dust polarization is a reliable tracer of magnetic fields in the diffuse ISM to molecular clouds to star-forming regions.

Dust polarization has been used widely to measure magnetic fields in star-forming regions when combined with DCF method. This enables us to quantify the role of magnetic fields in the star formation process (see Pattle and Fissel, 2019 for a recent review). Here, we discuss our recent study using dust polarization to measure magnetic fields in two star-forming regions discussed in Section 4 with SOFIA/HAWC+.

a) Mean magnetic field strength in M17

Knowing the variation of the magnetic fields (i.e., characterized by the polarization angle θ) induced by magnetically aligned dust grains, we can estimate the field strength using the DCF method as follows:

$$B_{\text{mean}} = f_{\text{DCF}} \sqrt{4\pi\rho} \frac{\delta_v}{\delta_\theta} \quad (49)$$

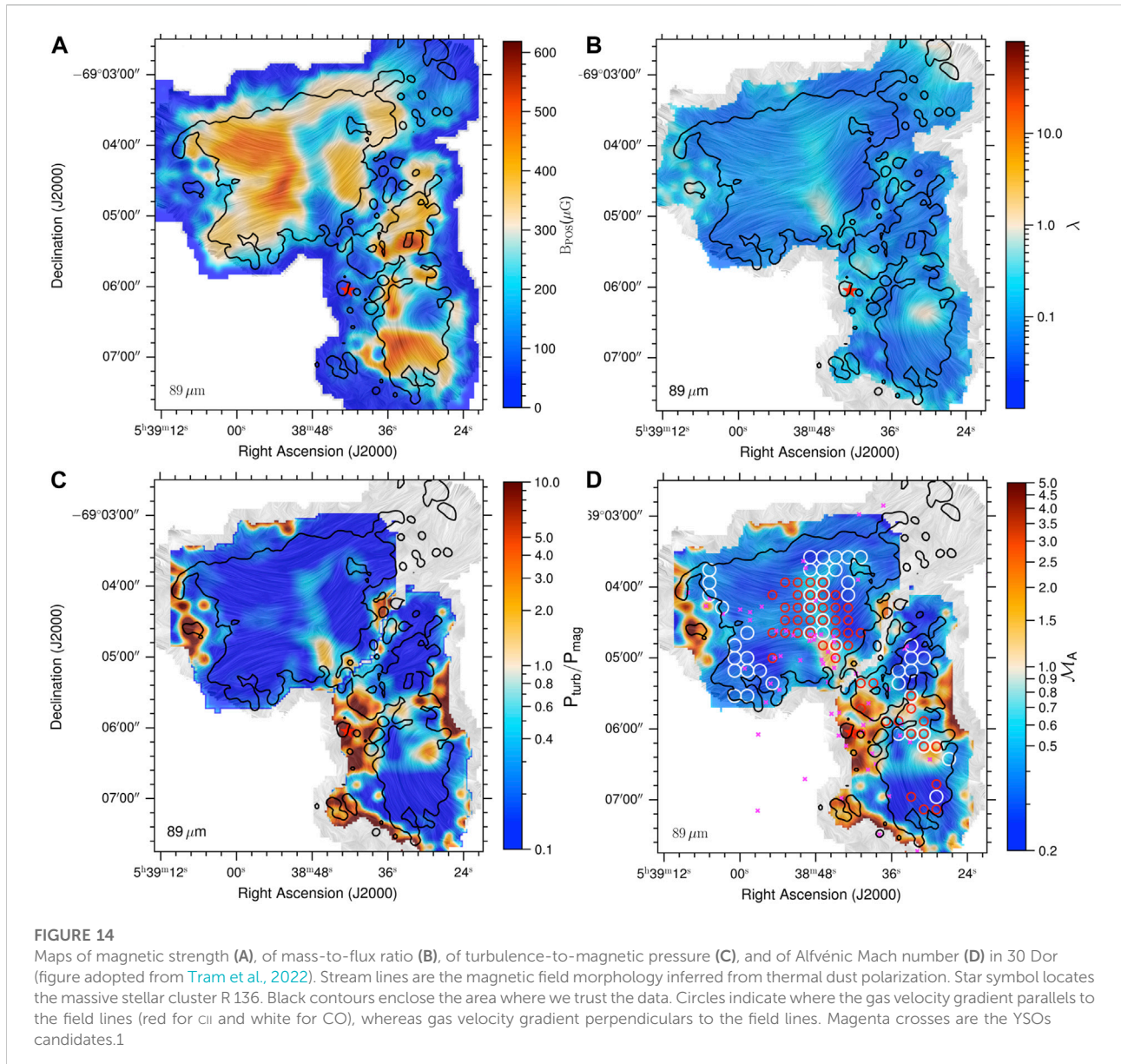
where f_{DCF} is a factor adjusting for line-of-sight and beam-integration effects, ρ is the gas mass density, δ_v is the dispersion in velocity of non-thermal gas, and δ_θ is the one

for polarization angle. The dispersion of non-thermal gas is derived from spectral lines of gas tracer, whereas we followed an modification made by Hildebrand et al. (2009) and Houde et al. (2009) that one replaces $\delta_\theta \rightarrow D_\theta^{1/2}$ with D_θ the structure function of θ to estimate the polarization angle dispersion. We constrained the field strengths are around $980 \pm 230 \mu\text{G}$ in M17-N and $1665 \pm 885 \mu\text{G}$ in M17-S. The mean value of the Alfvénic Mach number (\mathcal{M}_A) and the mass-to-flux ratio (λ) are consequently lower than 1, indicating that M17 is sub-Alfvénic and sub-critical or the magnetic fields are stronger than the turbulence and able to resist against gravitational collapse. Our constraints are consistent with the low starformation efficiency in M17 (see Hoang et al., 2022b for details computations).

b) Variation of magnetic field strength in 30 Dor

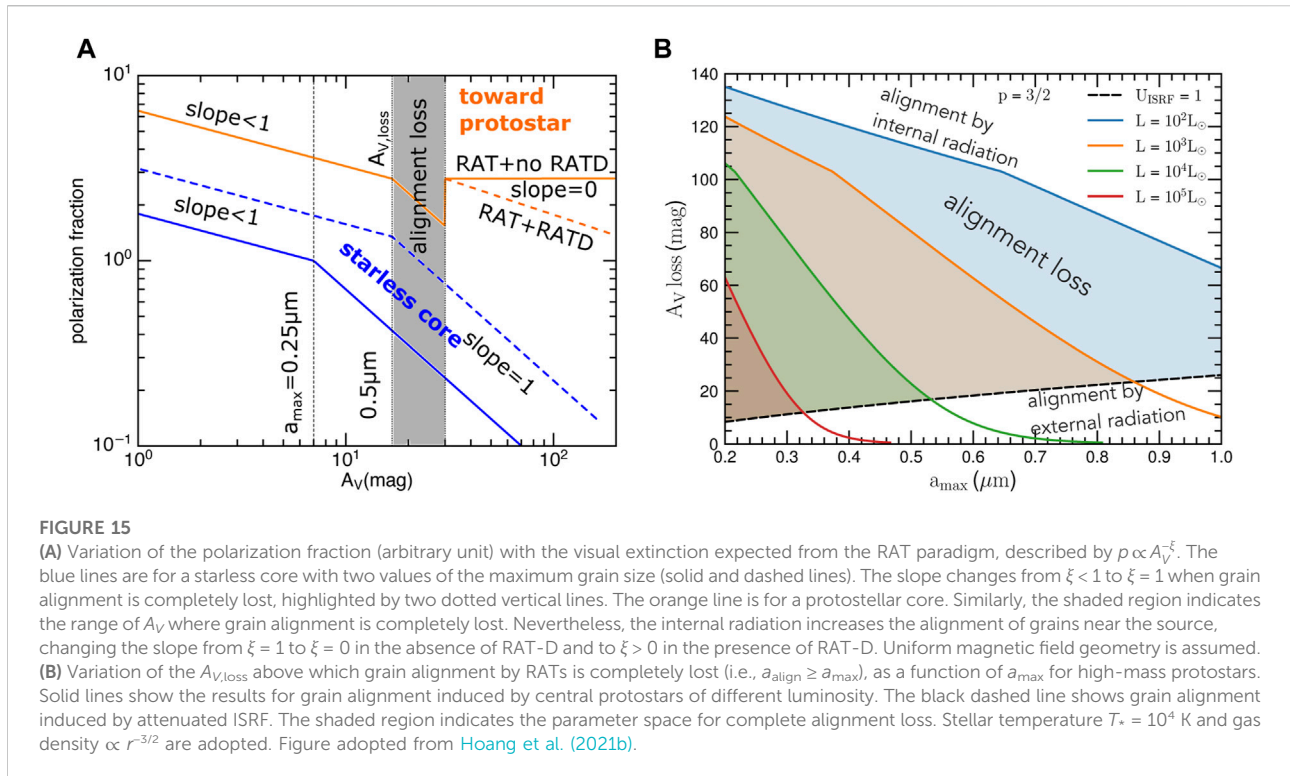
The DCF method expressed in Eq. 49 can be used to make maps of magnetic field strength (see Guerra et al., 2021). The maps of ρ , δ_v and D_θ are naturally required. The map of ρ is due to the width of cloud, which could be determined by the half-width at half-maximum of the polarized flux autocorrelation function (see e.g., Figure 1 in Houde et al., 2009). The map of δ_v is done by using a position-position-velocity datacube, whereas that of D_θ is acquired within a circular kernel of radius w (see Section 3.2 in Guerra et al., 2021 for a critical selection of a best kernel size).

Figure 14 shows the case of 30 Dor as an example. The magnetic field morphology (stream lines) is inferred from SOFIA/HAWC + observations (Tram et al., 2021b, 2022), which illustrates a complex but ordered structure. We



constructed a map of the magnetic strength using the DCF method (panel (a)), and found a quite strong field with a maximum of few hundred micro-Gauss. Consequently, most of the material associated with 30 Dor is 1) sub-critical (i.e., $\lambda < 1$, panel (b)), meaning that the magnetic field is stronger than gravity; and 2) sub-Alfvénic (i.e., $\mathcal{M}_A < 1$, panel (d)), meaning that magnetic field is stronger than turbulence, which is illustrated by the turbulence-to-magnetic pressure (panel (c)). Our estimation shows that magnetic field is strong enough to support the cloud against the feedback from the intense ionization source R 136. We compared the field morphology inferred from thermal dust polarization with that inferred from the velocity gradient technique (or VGT, see Hu et al., 2019, and

references therein), in which the velocity gradient is perpendicular to the ambient magnetic field. These two different techniques deliver different results at certain locations (located by the red and white circles in panel (d)) in 30 Dor. This disagreement implies that the velocity gradient is parallel to the field lines (or gas moves along the field) and gives evidence for local gravitational collapse (Hu et al., 2021). Because gas moves along the field, the gas motion is not affected by the magnetic pressure (which preferentially acts perpendicular to the field lines), and thus able to accumulate mass to trigger new stars to form in such a strong magnetic field. The locations of Young Stellar Objects are indicated by the magenta crosses for comparison.



5.2 Can thermal dust polarization trace magnetic fields in protostellar/ protoplanetary disks?

In very dense regions such as protostellar cores and disks, the process of grain alignment is far more complicated than in molecular clouds, as studied in detail in Hoang T. et al. (2022). A detailed modeling of grain alignment in a protoplanetary disk by Tazaki et al. (2017) shows that very large grains tend to align along the radiation direction (k-RAT) instead of the magnetic field (B-RAT). As pointed out in Hoang T. et al. (2022) their study, however, evaluated the radiative precession rate for grains at low $-J$ attractors, which overestimates the efficiency of k-RAT. They assumed that all grains have *right* internal alignment. This assumption is likely too simplistic knowing that grain alignment can be very complicated due to a complexity of gas density. Therefore, understanding both internal and external alignments of grains becomes the key to interpret dust polarization in protostellar environments (Hoang T. et al. 2022).

(Sub)millimeter polarization observations of protostars (e.g., Zhang et al., 2014; Cox et al., 2018; Sadavoy et al., 2019) showed that the pattern of thermal dust polarization is complicated and diverse. Thus, we need to establish a robust understanding of grain alignment in dense regions in order to interpret observations in a reliable way (whether or not the observed patterns actually trace magnetic fields). Detailed theoretical studies (Hoang T. et al., 2022) and numerical

modeling (Giang et al. in preparation) indicate that thermal dust polarization does not always trace magnetic fields under such conditions. A diversity of polarization patterns can be the result of multiple alignment mechanisms, and inferring the magnetic field from rotating polarization vectors might lead to inaccurate conclusions (Hoang T. et al., 2022).

5.3 Polarization hole within the RAT paradigm

In this section, we review the polarization hole effect that is frequently reported in starless cores and protostars (e.g., Alves et al., 2014; Hull et al., 2014; Jones et al., 2015; Cox et al., 2018; Pattle and Fissel, 2019) in the context of the RAT paradigm. As shown in Section 3, the alignment size a_{align} and maximum size a_{max} are keys in determining the polarization degree of thermal dust emission. These sizes are, in turn, determined by the properties of radiation field and of environment (gas temperature and gas density). In the following we consider sources with different physical conditions, including starless cores and protostellar cores.

For simplicity's sake, we also assume all grains have efficient internal alignment. Note that grain alignment under such conditions is much more complicated due to the complex gas density profile and interplay between different alignment mechanisms as discussed in Section 5.2.

Figure 15A shows the expected polarization degree versus the visual extinction from the cloud surface of a starless core (blue lines) and a protostellar core (orange line) within the RAT paradigm.

- For a starless core (a cloud is illuminated by the interstellar radiation field (ISRF) and has no embedded sources), grain alignment is controlled by this external field. The grain alignment becomes less efficient deeper inside the cloud due to the attenuation of the ISRF and increase of gas damping. The polarization degree gradually decreases with A_V . Once the minimum aligned grain size is larger than the maximum grain size ($a_{\text{align}} > a_{\text{max}}$), all grains completely lost their alignment, resulting at $p \sim A_V^{-1}$. Thus, the location ($A_{V,\text{loss}}$) where grain alignment is lost depends on a_{max} (vertical lines).
- For a protostellar core, there is an internal radiation source located at within of the cloud, in addition to the external interstellar radiation field. The polarization degree similarly gradually decreases as $p \sim A_V^{-\text{slope}}$ with a slope < 1 before the slope becomes 1 due to the loss of grain alignment by the ISRF. In the vicinity of the protostar, owing to the effect of the protostellar radiation, more small grains become aligned by RATs. The polarization degree is hence expected to increase monotonically (or at least stay constant when all grains are brought to align) toward the protostar. If the RAT-D mechanism occurs near the central star, the polarization degree is predicted to decrease instead of increase (dashed orange line).

Figure 15B shows the region from the cloud surface where grains are completely lost their alignment ($A_{V,\text{loss}}$) in the case of a massive protostar. It is determined by both the internal and external radiation fields. For a given maximum grain size, the more luminous source, the narrower $A_{V,\text{loss}}$, because this intense radiation field could align grains closer to the cloud surface by RATs. For a given luminosity, one can expect to have a similar narrower in range of $A_{V,\text{loss}}$ for larger grain size, because the RAT alignment efficiency is proportional to grain size as shown in Section 2.3. For a starless core, as mentioned, $A_{V,\text{loss}}$ is only dependent on the maximum grain size which implies that the observed polarization hole could help to constrain grain growth in such a condition.

5.4 Effects of RAT-A and RAT-D on grain growth and evolution, and observations

Grain growth is thought to occur in molecular clouds where grain alignment is ubiquitous as revealed by dust polarization. Therefore, the process of grain growth must involve the growth of aligned grains. Hoang (2022) suggested that the alignment of dust grains with ambient magnetic fields has an important effect

on grain growth in molecular clouds. Due to grain alignment, the process of grain growth via gas accretion and grain–grain collisions is anisotropic instead of isotropic as induced by Brownian random motions. As a result, large grains grown by gas accretion are expected to have elongation increasing with its radius. Moreover, dust aggregates formed by grain–grain collisions contain binary structures with aligned axes (Hoang, 2022), which is recently reported in primitive interplanetary dust grains (Hu and Winarski, 2021).

On the other hand, the RAT-D induces the change of the grain size distribution, depending on the local radiation field and gas densities (Hoang, 2021b). This disruption affects both the upper cutoff size and the abundance of smaller grains (including nanoparticles), and hence imprints on dust extinction, emission and polarization. The RAT-D effect is also important for grain surface chemistry, including rapid desorption of ice mantles, enhancement of thermal desorption of water and COMs. Therefore, the effect of RAT-A and RAT-D on the grain evolution can be accessible from observations in a large window from optical-UV to infrared to radio wavelengths (see Hoang, 2020 for a review).

5.5 Effects of RAT-A and RAT-D in the era of time-domain astrophysics

Dust grains in the local environment of transient sources (as supernovae, kilonovae, and gamma-ray bursts) can be transiently illuminated by an intense radiation flash from the source and are transiently aligned by RAT with both high $-J$ and low $-J$ attractor (fast RAT alignment). The efficiency of fast RAT alignment and disruption is determined by $f_{\text{high-}J}^{\text{fast}}$. The exact value of $f_{\text{high-}J}^{\text{fast}}$ depends on the grain properties (shape and size) and magnetic susceptibility. For grains consisting of ordinary paramagnetic material (e.g., silicate), Herranen et al. (2021) found that $f_{\text{high-}J}$ can be about 10–70% based on calculations of RATs for an ensemble of Gaussian random shapes.

Therefore, a fraction $f_{\text{high-}J}^{\text{fast}}$ of grains with size $a > a_{\text{disr}}$ can be disrupted into fragments. However, the fraction $1 - f_{\text{high-}J}$ grains aligned at low $-J$ attractors are not disrupted by RAT-D. Therefore, in the presence of RAT-D, large grains at $a > a_{\text{disr}}$ now can only rotate thermally at low $-J$ attractors. This selective disruption has an important implication for grain alignment and dust polarization. This results in a significant change in the grain size distribution and dust properties in the local environment of transients (Giang et al., 2020; Hoang et al., 2020). Since the RAT-D process is time-dependent, the optical and polarization properties of transient sources would change with time just because of the change in foreground dust. This is an important effect that needs to be accounted for to infer the intrinsic properties of SNe before their luminosity and colors can be used for cosmological studies of dark energy (Giang et al., 2020).

We note that the RAT-A and RAT-D effects also work for dust around other transient sources, including nova, episodic protostars, and AGN, which will be quantified in our future works.

5.6 Mechanical torque (MET) alignment

Lazarian and Hoang (2007b) and Hoang et al. (2018) realized that a gas flow could act to spin-up and align an irregular grain via the so-called mechanical torques (or METs). Instead of the effect of photons, as in the RAT paradigm, METs arises from the scattering of gas atoms by the grain surface that drifts through the ambient gas with the speed v_d . The suprathermal number of a grain spun-up by METs is given by (Hoang T. et al., 2022)

$$St_{\text{MET}} \approx 0.86\hat{\rho}^{1/2}s_{d,-1}^2a^{3/2}\left(\frac{s^{3/2}Q_{\text{spinup},-3}}{\Gamma_{\parallel}}\right), \quad (50)$$

where $s_d = v_d/v_T$ with v_T the thermal gas velocity ($s_{d,-1} = s_d/0.1$), and $Q_{\text{spinup},-3} = Q_{\text{spinup}}/10^{-3}$ is the spin-up efficiency. Here $Q_{\text{spinup}} = 0$ for a spherical grain, whereas $Q_{\text{spinup}} = 10^{-6} - 10^{-3}$ for irregular shapes (Hoang et al., 2018).

Interestingly, one can realize that St_{MET} is independent to the gas density, and only depends on the grain properties and drift velocity. It differs from the corresponding value for the RATs, which is less efficient in dense gas due to the gas damping. Comparing St_{MET} to St_{RAT} from Section 2.3, we see that METs are more important than RATs for only the very small grains (e.g., $a \leq 0.02 \mu\text{m}$ for $U = 10^6$ and $s_d = 0.5$) and for low density ($n_{\text{H}} = 10^3 \text{ cm}^{-3}$). In higher density ($n_{\text{H}} = 10^8 \text{ cm}^{-3}$), the effect of RATs is reduced significantly so that METs become dominant mechanism to spin-up grains. Therefore, METs play an important role in dense regions (e.g., protostellar cores or disks) as shown in Hoang T. et al. (2022). Similar to RATs, grains at low $-J$ attractors induced by METs are likely to precess around the gas flow \mathbf{v} , the so-called v -MET. Whereas grains at high $-J$ attractors are likely experienced in precessing around \mathbf{B} , the so-called B-MET. Therefore, the grain alignment and induced polarization due to METs need to be considered in modeling or simulation for a better interpretation of observations, as well as understanding physical properties of dust grain in such conditions.

References

- Ajeddig, H., Adam, R., Ade, P., André, P., Artis, E., Aussen, H., et al. (2022). "Probing the role of magnetic fields in star-forming filaments: NIKA2-Pol commissioning results toward OMC-1," in European Physical Journal Web of Conferences 257, 00002. arXiv:2111.14533. doi:10.1051/epjconf/202225700002
- Alves, F. O., Frau, P., Girart, J. M., Franco, G. A. P., Santos, F. P., and Wiesemeyer, H. (2014). On the radiation driven alignment of dust grains: Detection of the polarization hole in a starless core. *Astron. Astrophys.* 569, L1. doi:10.1051/0004-6361/201424678
- Andersson, B. G., Lazarian, A., and Vaillancourt, J. E. (2015). Interstellar dust grain alignment. *Annu. Rev. Astron. Astrophys.* 53, 501–539. doi:10.1146/annurev-astro-082214-122414

Author contributions

TH led the theory part and LT led the observational data analysis part of the manuscript. LT wrote the first draft of the manuscript. TH outlined and revised significantly the manuscript. Both authors contributed to manuscript writing, revision, read, and approved the manuscript.

Funding

TH was funded by the National Research Foundation of Korea (NRF) grant funded by the Korean government (MSIT) (No. 2019R1A2C1087045).

Acknowledgments

We are grateful to the referees for helpful comments that improved our manuscript. We thank Karl Menten and Helmut Wiesemeyer for careful proof reading and comments, Nguyen Chau Giang and Nguyen Thi Phuong for useful suggestions, and Nguyen Bich Ngoc for allowing us to use her preliminary results.

Conflict of interest

The authors declare that the research was conducted in the absence of any commercial or financial relationships that could be construed as a potential conflict of interest.

Publisher's note

All claims expressed in this article are solely those of the authors and do not necessarily represent those of their affiliated organizations, or those of the publisher, the editors, and the reviewers. Any product that may be evaluated in this article, or claim that may be made by its manufacturer, is not guaranteed or endorsed by the publisher.

- Arzoumanian, D., Furuya, R. S., Hasegawa, T., Tahani, M., Sadavoy, S., Hull, C. L. H., et al. (2021). Dust polarized emission observations of NGC 6334. BISTRO reveals the details of the complex but organized magnetic field structure of the high-mass star-forming hub-filament network. *Astron. Astrophys.* 647, A78. doi:10.1051/0004-6361/202038624

- Barnett, S. J. (1909). On magnetization by angular acceleration. *Science* 30 (769), 413. doi:10.1126/science.30.769.413

- Batria, W., Wilson, T., Bastien, P., and Ruf, K. (1983). Clumping in molecular clouds—the region between omc 1 and 2. *Astron. Astrophys.* 128, 279–290.

- Becklin, E., and Neugebauer, G. (1967). Observations of an infrared star in the orion nebula. *Astrophys. J.* 147, 799. doi:10.1086/149055

- Bisschop, S. E., Jørgensen, J. K., van Dishoeck, E. F., and de Wachter, E. B. M. (2007). Testing grain-surface chemistry in massive hot-core regions. *Astron. Astrophys.* 465, 913–929. doi:10.1051/0004-6361:20065963
- Blake, G. A., Sutton, E. C., Masson, C. R., and Phillips, T. G. (1987). Molecular abundances in OMC-1: The chemical composition of interstellar molecular clouds and the influence of massive star formation. *Astrophys. J.* 315, 621. doi:10.1086/165165
- Borlaff, A. S., Lopez-Rodriguez, E., Beck, R., Stepanov, R., Ntormousi, E., Hughes, A., et al. (2021). Extragalactic magnetism with SOFIA (legacy program). I. The magnetic field in the multiphase interstellar medium of M51. *Astrophys. J.* 921, 128. doi:10.3847/1538-4357/ac16d7
- Brown, P. D., Charnley, S. B., and Millar, T. J. (1988). A model of the chemistry in hot molecular cores. *Mon. Not. R. Astron. Soc.* 231, 409–417. doi:10.1093/mnras/231.2.409
- Chandrasekhar, S., and Fermi, E. (1953). Magnetic fields in spiral arms. *Astrophys. J.* 118, 113. doi:10.1086/145731
- Chini, R. (1981). Multicolour photometry of stars in the Ophiuchus dark cloud region. *Astron. Astrophys.* 99, 346–350.
- Chuss, D. T., Andersson, B. G., Bally, J., Dotson, J. L., Dowell, C. D., Guerra, J. A., et al. (2019). HAWC+/SOFIA multiwavelength polarimetric observations of OMC-1. *Astrophys. J.* 872, 187. doi:10.3847/1538-4357/aafd37
- Compiègne, M., Verstraete, L., Jones, A., Bernard, J. P., Boulanger, F., Flagey, N., et al. (2011). The global dust SED: Tracing the nature and evolution of dust with DustEM. *Astron. Astrophys.* 525, A103. doi:10.1051/0004-6361/201015292
- Coudé, S., Bastien, P., Houde, M., Sadavoy, S., Friesen, R., Di Francesco, J., et al. (2019). The JCMT BISTRO survey: The magnetic field of the barnard 1 star-forming region. *Astrophys. J.* 877, 88. doi:10.3847/1538-4357/ab1b23
- Cox, E. G., Harris, R. J., Looney, L. W., Li, Z.-Y., Yang, H., Tobin, J. J., et al. (2018). ALMA's polarized view of 10 protostars in the perseus molecular cloud. *Astrophys. J.* 855, 92. doi:10.3847/1538-4357/aaacd2
- Crutcher, R. M. (2012). Magnetic fields in molecular clouds. *Annu. Rev. Astron. Astrophys.* 50, 29–63. doi:10.1146/annurev-astro-081811-125514
- Curran, R. L., and Chrysostomou, A. (2007). Magnetic fields in massive star-forming regions. *Mon. Not. R. Astron. Soc.* 382, 699–716. doi:10.1111/j.1365-2966.2007.12399.x
- Davis, J. L., Jr, and Greenstein, J. L. (1951). The polarization of starlight by aligned dust grains. *Astrophys. J.* 114, 206. doi:10.1086/145464
- Davis, L. (1951). The strength of interstellar magnetic fields. *Phys. Rev.* 81, 890–891. doi:10.1103/PhysRev.81.890.2
- De Buizer, J. M., Morris, M. R., Becklin, E. E., Zinnecker, H., Herter, T. L., Adams, J. D., et al. (2012). First science observations with SOFIA/FORCAST: 6–37 μm imaging of orion BN/KL. *Astrophys. J.* 749, L23. doi:10.1088/2041-8205/749/2/L23
- de Geus, E. J., de Zeeuw, P. T., and Lub, J. (1989). Physical parameters of stars in the Scorpio-Centaurus OB association. *Astron. Astrophys.* 216, 44–61.
- De Marchi, G., Paresce, F., Panagia, N., Beccari, G., Spezzi, L., Sirianni, M., et al. (2011). star formation in 30 Doradus. *Astrophys. J.* 739, 27. doi:10.1088/0004-637X/739/1/27
- Devaraj, R., Clemens, D. P., Dewangan, L. K., Luna, A., Ray, T. P., and Mackey, J. (2021). Magnetic fields and star formation around H II regions: The S235 complex. *Astrophys. J.* 911, 81. doi:10.3847/1538-4357/abe9b1
- Doi, Y., Hasegawa, T., Furuya, R. S., Coudé, S., Hull, C. L. H., Arzoumanian, D., et al. (2020). The JCMT BISTRO survey: Magnetic fields associated with a network of filaments in NGC 1333. *Astrophys. J.* 899, 28. doi:10.3847/1538-4357/abae2
- Dolginov, A. Z., and Mitrofanov, I. G. (1976). Orientation of cosmic dust grains. *Astrophys. Space Sci.* 43, 291–317. doi:10.1007/BF00640010
- Draine, B. T., and Flatau, P. J. (1994). Discrete-dipole approximation for scattering calculations. *J. Opt. Soc. Am. A* 11, 1491–1499. doi:10.1364/JOSAA.11.001491
- Draine, B. T., and Flatau, P. J. (2008). Discrete-dipole approximation for periodic targets: Theory and tests. *J. Opt. Soc. Am. A* 25, 2693. doi:10.1364/JOSAA.25.002693
- Draine, B. T., and Friauf, A. A. (2009). Polarized far-infrared and submillimeter emission from interstellar dust. *Astrophys. J.* 696, 1–11. doi:10.1088/0004-637X/696/1/1
- Draine, B. T., and Hensley, B. S. (2021). The dielectric function of “astrodust” and predictions for polarization in the 3.4 and 10 μm features. *Astrophys. J.* 909, 94. doi:10.3847/1538-4357/abd6c6
- Draine, B. T., and Weingartner, J. C. (1996). Radiative torques on interstellar grains. I. Superthermal spin-up. *Astrophys. J.* 470, 551. doi:10.1086/177887
- Draine, B. T., and Weingartner, J. C. (1997). Radiative torques on interstellar grains. II. Grain alignment. *Astrophys. J.* 480, 633–646. doi:10.1086/304008
- Draine, B. T. (2011). *Physics of the interstellar and intergalactic medium*. Preprint to arXiv.
- Dufour, R. J., Shields, G. A., and Talbot, R. J., Jr (1982). The carbon abundance in the Magellanic Clouds from IUE observations of H II regions. *Astrophys. J.* 252, 461–473. doi:10.1086/159574
- Efroimsky, M., and Lazarian, A. (2000). Inelastic dissipation in wobbling asteroids and comets. *Mon. Not. R. Astron. Soc.* 311, 269–278. doi:10.1046/j.1365-8711.2000.03036.x
- Einstein, A., and de Haas, W. J. (1915). Experimental proof of the existence of Ampère's molecular currents. *K. Ned. Akad. Wet. Proceed. Series B Phys. Sci.* 18, 696–711.
- Flatau, P. J., and Draine, B. T. (2012). Fast near field calculations in the discrete dipole approximation for regular rectilinear grids. *Opt. Express* 20, 1247. doi:10.1364/OE.20.001247
- Friberg, P., Berry, D., Savini, G., Bintley, D., Dempsey, J., Graves, S., et al. (2018). “Characterizing and reducing the POL-2 instrumental polarization,” in *Millimeter, submillimeter, and far-infrared detectors and instrumentation for astronomy IX*. Editors J. Zmuidzinas and J.-R. Gao, 10708, 107083M. Society of Photo-Optical Instrumentation Engineers (SPIE) Conference Series. doi:10.1117/12.2314345
- Galitzki, N., Ade, P. A. R., Angilè, F. E., Benton, S. J., Devlin, M. J., Dober, B., et al. (2014). “The balloon-borne large aperture submillimeter telescope for polarimetry-BLASTPOL: performance and results from the 2012 antarctic flight,” in *Ground-based and airborne telescopes V*. Editors L. M. Stepp, R. Gilmozzi, and H. J. Hall, 9145, 91450R. Society of Photo-Optical Instrumentation Engineers (SPIE) Conference Series. doi:10.1117/12.2054759
- Galliano, F., Madden, S. C., Tielens, A. G. G. M., Peeters, E., and Jones, A. P. (2008). Variations of the mid-IR aromatic features inside and among galaxies. *Astrophys. J.* 679, 310–345. doi:10.1086/587051
- Garrod, R. T., Widicus Weaver, S. L., and Herbst, E. (2008). Complex chemistry in star-forming regions: An expanded gas-grain warm-up chemical model. *Astrophys. J.* 682, 283–302. doi:10.1086/588035
- Giang, N. C., Hoang, T., and Tram, L. N. (2020). Time-varying extinction, polarization, and colors of type Ia supernovae due to rotational disruption of dust grains. *Astrophys. J.* 888, 93. doi:10.3847/1538-4357/ab5d37
- Goodman, A. A., Jones, T. J., Lada, E. A., and Myers, P. C. (1992). The structure of magnetic fields in dark clouds: Infrared polarimetry in B216–217. *Astrophys. J.* 399, 108. doi:10.1086/171907
- Goodman, A. A., Jones, T. J., Lada, E. A., and Myers, P. C. (1995). Does near-infrared polarimetry reveal the magnetic field in cold dark clouds? *Astrophys. J.* 448, 748. doi:10.1086/176003
- Guerra, J. A., Chuss, D. T., Dowell, C. D., Houde, M., Michail, J. M., Siah, J., et al. (2021). Maps of magnetic field strength in the OMC-1 using HAWC+ FIR polarimetric data. *Astrophys. J.* 908, 98. doi:10.3847/1538-4357/abd6f0
- Guillet, V., Fanciullo, L., Verstraete, L., Boulanger, F., Jones, A. P., Miville-Deschênes, M. A., et al. (2018). Dust models compatible with Planck intensity and polarization data in translucent lines of sight. *Astron. Astrophys.* 610, A16. doi:10.1051/0004-6361/201630271
- Hall, J. S. (1949). Observations of the polarized light from stars. *Science* 109, 166–167. doi:10.1126/science.109.2825.166
- Hamaguchi, K., Corcoran, M. F., and Imanishi, K. (2003). Chandra observations of a young embedded magnetic B star in the ρ Ophiuchus cloud. *Publ. Astron. Soc. Jpn. Nihon. Tenmon. Gakkai.* 55, 981–987. doi:10.1093/pasj/55.5.981
- Harper, D. A., Runyan, M. C., Dowell, C. D., Wirth, C. J., Amato, M., Ames, T., et al. (2018). HAWC+, the far-infrared camera and polarimeter for SOFIA. *J. Astron. Instrum.* 7, 1840008–1841025. doi:10.1142/S2251171718400081
- Heiles, C., and Crutcher, R. (2005). “Magnetic fields in diffuse HI and molecular clouds,” in *Cosmic magnetic fields*. Editors R. Wielebinski and R. Beck, 664, 137. doi:10.1007/11369875_7
- Herranen, J., Lazarian, A., and Hoang, T. (2021). Alignment of irregular grains by radiative torques: Efficiency study. *Astrophys. J.* 913, 63. doi:10.3847/1538-4357/abf096
- Hildebrand, R. H., Kirby, L., Dotson, J. L., Houde, M., and Vaillancourt, J. E. (2009). Dispersion of magnetic fields in molecular clouds. I. *Astrophys. J.* 696, 567–573. doi:10.1088/0004-637X/696/1/567
- Hildebrand, R. H. (1988). Magnetic fields and stardust. *Q. J. R. Astron. Soc.* 29, 327–351.
- Hiltner, W. A. (1949). Polarization of light from distant stars by interstellar medium. *Science* 109, 165. doi:10.1126/science.109.2825.165
- Hirashita, H., and Hoang, T. (2020). Effects of rotational disruption on the evolution of grain size distribution in galaxies. *Mon. Not. R. Astron. Soc.* 494, 1058–1070. doi:10.1093/mnras/staa793

- Hoang, T., and Lazarian, A. (2008). Radiative torque alignment: Essential physical processes. *Mon. Not. R. Astron. Soc.* 388, 117–143. doi:10.1111/j.1365-2966.2008.13249.x
- Hoang, T., and Lazarian, A. (2009). Radiative torques alignment in the presence of pinwheel torques. *Astrophys. J.* 695, 1457–1476. doi:10.1088/0004-637X/695/2/1457
- Hoang, T., and Lazarian, A. (2014). Grain alignment by radiative torques in special conditions and implications. *Mon. Not. R. Astron. Soc.* 438, 680–703. doi:10.1093/mnras/stt2240
- Hoang, T., and Lazarian, A. (2016a). A unified model of grain alignment: Radiative alignment of interstellar grains with magnetic inclusions. *Astrophys. J.* 831, 159. doi:10.3847/0004-637X/831/2/159
- Hoang, T., and Lazarian, A. (2016b). Polarization of magnetic dipole emission and spinning dust emission from magnetic nanoparticles. *Astrophys. J.* 821, 91. doi:10.3847/0004-637X/821/2/91
- Hoang, T., and Tram, L. N. (2020). Rotational desorption of ice mantles from suprathermally rotating grains around young stellar Objects. *Astrophys. J.* 891, 38. doi:10.3847/1538-4357/ab6eff
- Hoang, T., and Tung, N.-D. (2020). Evolution of dust and water ice in cometary comae by radiative torques. *Astrophys. J.* 901, 59. doi:10.3847/1538-4357/abafa5
- Hoang, T., Lazarian, A., and Martin, P. G. (2014). Paramagnetic alignment of small grains: A novel method for measuring interstellar magnetic fields. *Astrophys. J.* 790, 6. doi:10.1088/0004-637X/790/1/6
- Hoang, T., Cho, J., and Lazarian, A. (2018). Alignment of irregular grains by mechanical torques. *Astrophys. J.* 852, 129. doi:10.3847/1538-4357/aa9edc
- Hoang, T., Tram, L. N., Lee, H., and Ahn, S.-H. (2019). Rotational disruption of dust grains by radiative torques in strong radiation fields. *Nat. Astron.* 3, 766–775. doi:10.1038/s41550-019-0763-6
- Hoang, T., Giang, N. C., and Tram, L. N. (2020). Gamma-ray burst Afterglows: Time-varying extinction, polarization, and colors due to rotational disruption of dust grains. *Astrophys. J.* 895, 16. doi:10.3847/1538-4357/ab8ae1
- Hoang, T., Lazarian, A., Lee, H., Cho, K., Gu, P.-G., and Ng, C.-H. (2021a). Effect of dust rotational disruption by radiative torques and implications for the F-corona decrease revealed by the parker solar probe. *Astrophys. J.* 919, 91. doi:10.3847/1538-4357/ac126e
- Hoang, T., Tram, L. N., Lee, H., Diep, P. N., and Ngoc, N. B. (2021b). Grain alignment and disruption by radiative torques in dense molecular clouds and implication for polarization holes. *Astrophys. J.* 908, 218. doi:10.3847/1538-4357/abd54f
- Hoang, T., Tram, L. N., Phan, V. H. M., Chau Giang, N., Phuong, N. T., and Dieu, N. D. (2022a). *On internal and external alignment of dust grains in protostellar environments.* arXiv:2205.02334.
- Hoang, T. D., Ngoc, N. B., Diep, P. N., Tram, L. N., Hoang, T., Pattle, K., et al. (2022b). Studying magnetic fields and dust in M17 using polarized thermal dust emission observed by SOFIA/HAWC+. *Astrophys. J.* 929, 27. doi:10.3847/1538-4357/ac5abf
- Hoang, T. (2019). A dynamical constraint on interstellar dust models from radiative torque disruption. *Astrophys. J.* 876, 13. doi:10.3847/1538-4357/ab1075
- Hoang, T. (2020). Rotational disruption of astrophysical dust and ice—theory and applications. *Galaxies* 8, 52. doi:10.3390/galaxies8030052
- Hoang, T. (2021a). Effect of dust rotational disruption by radiative torques on radiation pressure feedback from massive protostars. *Astrophys. J.* 921, 21. doi:10.3847/1538-4357/ac185d
- Hoang, T. (2021b). Variation of dust properties with cosmic time implied by radiative torque disruption. *Astrophys. J.* 907, 37. doi:10.3847/1538-4357/abccc8
- Hoang, T. (2022). Effects of grain alignment with magnetic fields on grain growth and the structure of dust aggregates. *Astrophys. J.* 928, 102. doi:10.3847/1538-4357/ac5408
- Houde, M., Vaillancourt, J. E., Hildebrand, R. H., Chitsazzadeh, S., and Kirby, L. (2009). Dispersion of magnetic fields in molecular clouds. II. *Astrophys. J.* 706, 1504–1516. doi:10.1088/0004-637X/706/2/1504
- Hu, Z. W., and Winarski, R. P. (2021). Elementary composite binary and grain alignment locked in dust growth. *Astrophys. J. Lett.* 923, L4. doi:10.3847/2041-8213/ac391e
- Hu, Y., Yuen, K. H., Lazarian, V., Ho, K. W., Benjamin, R. A., Hill, A. S., et al. (2019). Magnetic field morphology in interstellar clouds with the velocity gradient technique. *Nat. Astron.* 3, 776–782. doi:10.1038/s41550-019-0769-0
- Hu, Y., Lazarian, A., and Stanimirović, S. (2021). Revealing gravitational collapse in the serpens G3-G6 molecular cloud using velocity gradients. *Astrophys. J.* 912, 2. doi:10.3847/1538-4357/abedb7
- Hull, C. L. H., and Plambeck, R. L. (2015). The 1.3mm full-Stokes polarization system at CARMA. *J. Astron. Instrum.* 4, 1550005. doi:10.1142/S2251171715500051
- Hull, C. L. H., Plambeck, R. L., Kwon, W., Bower, G. C., Carpenter, J. M., Crutcher, R. M., et al. (2014). TADPOL: A 1.3 mm survey of dust polarization in star-forming cores and regions. *Astrophys. J. Suppl. Ser.* 213, 13. doi:10.1088/0067-0049/213/1/13
- Jiménez-Serra, I., Vasyunin, A. I., Caselli, P., Marcelino, N., Billot, N., Viti, S., et al. (2016). The spatial distribution of complex organic molecules in the L1544 pre-stellar core. *Astrophys. J.* 830, L6. doi:10.3847/2041-8205/830/1/L6
- Jones, R. V., and Spitzer, L., Jr (1967). Magnetic alignment of interstellar grains. *Astrophys. J.* 147, 943. doi:10.1086/149086
- Jones, T. J., Klebe, D., and Dickey, J. M. (1992). Infrared polarimetry and the galactic magnetic field. II. Improved models. *Astrophys. J.* 389, 602. doi:10.1086/171233
- Jones, A. P., Fanciullo, L., Köhler, M., Verstraete, L., Guillet, V., Bocchio, M., et al. (2013). The evolution of amorphous hydrocarbons in the ISM: dust modelling from a new vantage point. *Astron. Astrophys.* 558, A62. doi:10.1051/0004-6361/2013121686
- Jones, T. J., Bagley, M., Krejny, M., Andersson, B. G., and Bastien, P. (2015). Grain alignment in starless cores. *Astron. J.* 149, 31. doi:10.1088/0004-6256/149/1/31
- Jones, T. J., Kim, J.-A., Dowell, C. D., Morris, M. R., Pineda, J. L., Benford, D. J., et al. (2020). HAWC+ far-infrared observations of the magnetic field geometry in M51 and NGC 891. *Astron. J.* 160, 167. doi:10.3847/1538-3881/abada8
- Kleinmann, D., and Low, F. (1967). Discovery of an infrared nebula in orion. *Astrophys. J.* 149, L1. doi:10.1086/180039
- Knapmeyer, M., Fischer, H.-H., Knollenberg, J., Seidensticker, K., Thiel, K., Arnold, W., et al. (2018). Structure and elastic parameters of the near surface of Abydos site on comet 67P/Churyumov–Gerasimenko, as obtained by SESAME/CASSE listening to the MUPUS insertion phase. *Icarus* 310, 165–193. doi:10.1016/j.icarus.2017.12.002
- Kounkel, M., Hartmann, L., Loinard, L., Ortiz-León, G. N., Mioduszewski, A. J., Rodríguez, L. F., et al. (2017). The Gould's belt distances survey (gobelins). ii. distances and structure toward the orion molecular clouds. *Astrophys. J.* 834, 142. doi:10.3847/1538-4357/834/2/142
- Kwon, W., Pattle, K., Sadavoy, S., Hull, C. L. H., Johnstone, D., Ward-Thompson, D., et al. (2022). B-fields in star-forming region observations (BISTRO): Magnetic fields in the filamentary structures of serpens main. *Astrophys. J.* 926, 163. doi:10.3847/1538-4357/ac4bbe
- Lazarian, A., and Draine, B. T. (1999). Nuclear spin relaxation within interstellar grains. *Astrophys. J.* 520, L67–L70. doi:10.1086/312137
- Lazarian, A., and Efrimsky, M. (1999). Inelastic dissipation in a freely rotating body: application to cosmic dust alignment. *Mon. Not. R. Astron. Soc.* 303, 673–684. doi:10.1046/j.1365-8711.1999.02235.x
- Lazarian, A., and Hoang, T. (2007a). Radiative torques: analytical model and basic properties. *Mon. Not. R. Astron. Soc.* 378, 910–946. doi:10.1111/j.1365-2966.2007.11817.x
- Lazarian, A., and Hoang, T. (2007b). Subsonic mechanical alignment of irregular grains. *Astrophys. J.* 669, L77–L80. doi:10.1086/523849
- Lazarian, A., and Hoang, T. (2008). Alignment of dust with magnetic inclusions: Radiative torques and superparamagnetic Barnett and nuclear relaxation. *Astrophys. J.* 676, L25–L28. doi:10.1086/586706
- Lazarian, A., and Hoang, T. (2021). Alignment and rotational disruption of dust. *Astrophys. J.* 908, 12. doi:10.3847/1538-4357/abd02c
- Lazarian, A., Andersson, B. G., and Hoang, T. (2015). “Grain alignment: Role of radiative torques and paramagnetic relaxation,” in *Polarimetry of stars and planetary systems*, 81.
- Lazarian, A. (2007). Tracing magnetic fields with aligned grains. *J. Quant. Spectrosc. Radiat. Transf.* 106, 225–256. doi:10.1016/j.jqsrt.2007.01.038
- Lee, H., Hoang, T., Le, N., and Cho, J. (2020). Physical model of dust polarization by radiative torque alignment and disruption and implications for grain internal structures. *Astrophys. J.* 896, 44. doi:10.3847/1538-4357/ab8e33
- Li, H., Dowell, C. D., Kirby, L., Novak, G., and Vaillancourt, J. E. (2008). Design and initial performance of SHARP, a polarimeter for the SHARC-II camera at the Caltech Submillimeter Observatory. *Appl. Opt.* 47, 422–430. doi:10.1364/AO.47.000422
- Lim, W., Buizer, J. M. D., and Radomski, J. T. (2020). Surveying the giant h ii regions of the milky way with SOFIA. II. m17. *Astrophys. J.* 888, 98. doi:10.3847/1538-4357/ab5fd0
- Lopez, L. A., Krumholz, M. R., Bolatto, A. D., Prochaska, J. X., and Ramirez-Ruiz, E. (2011). What drives the expansion of giant H II regions?: A study of stellar feedback in 30 Doradus. *Astrophys. J.* 731, 91. doi:10.1088/0004-637X/731/2/91

- Lopez-Rodriguez, E., Dowell, C. D., Jones, T. J., Harper, D. A., Berthoud, M., Chuss, D., et al. (2020). SOFIA/HAWC+ traces the magnetic fields in NGC 1068. *Astrophys. J.* 888, 66. doi:10.3847/1538-4357/ab5849
- Lopez-Rodriguez, E. (2021). The magnetic field across the molecular warped disk of Centaurus A. *Nat. Astron.* 5, 604–614. doi:10.1038/s41550-021-01329-9
- Marrone, D. P., and Rao, R. (2008). “The submillimeter array polarimeter,” in *Millimeter and submillimeter detectors and instrumentation for astronomy IV*. Editors W. D. Duncan, W. S. Holland, S. Withington, and J. Zmuidzinas 7020, 70202B. Society of Photo-Optical Instrumentation Engineers (SPIE) Conference Series. doi:10.1117/12.788677
- Mathis, J. S., Mezger, P. G., and Panagia, N. (1983). Interstellar radiation field and dust temperatures in the diffuse interstellar matter and in giant molecular clouds. *Astron. Astrophys.* 500, 259–276.
- Menten, K. M., Reid, M. J., Forbrich, J., and Brunthaler, A. (2007). The distance to the orion nebula. *Astron. Astrophys.* 474, 515–520. doi:10.1051/0004-6361/20078247
- Misawa, R., Bernard, J. P., Ade, P., André, Y., de Bernardis, P., Bouzit, M., et al. (2014). “Pilot: a balloon-borne experiment to measure the polarized FIR emission of dust grains in the interstellar medium,” in *Millimeter, submillimeter, and far-infrared detectors and instrumentation for astronomy VII*. Editors W. S. Holland and J. Zmuidzinas, 9153, 91531H. Society of Photo-Optical Instrumentation Engineers (SPIE) Conference Series. doi:10.1117/12.2055506
- Nagai, H., Nakanishi, K., Paladino, R., Hull, C. L. H., Cortes, P., Moellenbrock, G., et al. (2016). ALMA science verification data: Millimeter continuum polarimetry of the bright radio quasar 3C 286. *Astrophys. J.* 824, 132. doi:10.3847/0004-637X/824/2/132
- Ngoc, N. B., Diep, P. N., Parsons, H., Pattle, K., Hoang, T., Ward-Thompson, D., et al. (2021). Observations of magnetic fields surrounding LkHa 101 taken by the BISTRO survey with JCMT-POL-2. *Astrophys. J.* 908, 10. doi:10.3847/1538-4357/abd0fc
- Ortiz-León, G. N., Loinard, L., Kounkel, M. A., Dzib, S. A., Mioduszewski, A. J., Rodriguez, L. F., et al. (2017). The Gould’s belt distances survey (GOBELINS). I. Trigonometric parallax distances and depth of the Ophiuchus complex. *Astrophys. J.* 834, 141. doi:10.3847/1538-4357/834/2/141
- Pattle, K., and Fissel, L. (2019). Submillimeter and far-infrared polarimetric observations of magnetic fields in star-forming regions. *Front. Astron. Space Sci.* 6, 15. doi:10.3389/fspas.2019.00015
- Pattle, K., Ward-Thompson, D., Berry, D., Hatchell, J., Chen, H.-R., Pon, A., et al. (2017). The JCMT BISTRO survey: The magnetic field strength in the orion A filament. *Astrophys. J.* 846, 122. doi:10.3847/1538-4357/aa80e5
- Pattle, K., Lai, S.-P., Hasegawa, T., Wang, J.-W., Furuya, R. S., Ward-Thompson, D., et al. (2019). JCMT BISTRO survey observations of the Ophiuchus molecular cloud: Dust grain alignment properties inferred using a ricean noise model. *Astrophys. J.* 880, 27. doi:10.3847/1538-4357/ab286f
- Pattle, K., Gear, W., Redman, M., Smith, M. W. L., and Greaves, J. (2021a). Submillimeter observations of the two-component magnetic field in M82. *Mon. Not. R. Astron. Soc.* 505, 684–688. doi:10.1093/mnras/stab1300
- Pattle, K., Lai, S.-P., Wright, M., Coudé, S., Plambeck, R., Hoang, T., et al. (2021b). OMC-1 dust polarization in ALMA band 7: diagnosing grain alignment mechanisms in the vicinity of orion source I. *Mon. Not. R. Astron. Soc.* 503, 3414–3433. doi:10.1093/mnras/stab608
- Pattle, K., Fissel, L., Tahani, M., Liu, T., and Ntormousi, E. (2022). *Magnetic fields in star formation: from clouds to cores*. arXiv e-prints. arXiv:2203.11179.
- Pillai, T. G. S., Clemens, D. P., Reissl, S., Myers, P. C., Kauffmann, J., Lopez-Rodriguez, E., et al. (2020). Magnetized filamentary gas flows feeding the young embedded cluster in Serpens South. *Nat. Astron.* 4, 1195–1201. doi:10.1038/s41550-020-1172-6
- Planck Collaboration Ade, P. A. R., Aghanim, N., Alves, M. I. R., Armitage-Caplan, C., Arnaud, M., et al. (2014). Planck 2013 results. I. Overview of products and scientific results. *Astron. Astrophys.* 571, A1. doi:10.1051/0004-6361/201321529
- Planck Collaboration Ade, P. A. R., Aghanim, N., Alina, D., Alves, M. I. R., Armitage-Caplan, C., et al. (2015). Planck intermediate results. xix. an overview of the polarized thermal emission from galactic dust. *Astron. Astrophys.* 576, A104. doi:10.1051/0004-6361/201424082
- Planck Collaboration Aghanim, N., Akrami, Y., Alves, M. I. R., Ashdown, M., Aumont, J., et al. (2020). Planck 2018 results. XII. Galactic astrophysics using polarized dust emission. *Astron. Astrophys.* 641, A12. doi:10.1051/0004-6361/201833885
- Povich, M. S., Churchwell, E., Bieging, J. H., Kang, M., Whitney, B. A., Brogan, C. L., et al. (2009). THE EXTENDED ENVIRONMENT OF m17: A star formation history. *Astrophys. J.* 696, 1278–1306. doi:10.1088/0004-637x/696/2/1278
- Purcell, E. M. (1979). Suprathermal rotation of interstellar grains. *Astrophys. J.* 231, 404–416. doi:10.1086/157204
- Reissl, S., Wolf, S., and Brauer, R. (2016). Radiative transfer with POLARIS. I. Analysis of magnetic fields through synthetic dust continuum polarization measurements. *Astron. Astrophys.* 593, A87. doi:10.1051/0004-6361/201424930
- Roman-Duval, J., Gordon, K. D., Meixner, M., Bot, C., Bolatto, A., Hughes, A., et al. (2014). Dust and gas in the magellanic clouds from the HERITAGE Herschel key project. II. Gas-to-dust ratio variations across interstellar medium phases. *Astrophys. J.* 797, 86. doi:10.1088/0004-637X/797/2/86
- Sadavoy, S. I., Stephens, I. W., Myers, P. C., Looney, L., Tobin, J., Kwon, W., et al. (2019). Dust polarization toward embedded protostars in Ophiuchus with ALMA. III. Survey overview. *Astrophys. J. Suppl. Ser.* 245, 2. doi:10.3847/1538-4365/ab4257
- Santos, F. P., Chuss, D. T., Dowell, C. D., Houde, M., Looney, L. W., Lopez Rodriguez, E., et al. (2019). The far-infrared polarization spectrum of ρ ophiuchi A from HAWC+/SOFIA observations. *Astrophys. J.* 882, 113. doi:10.3847/1538-4357/ab3407
- Tazaki, R., Lazarian, A., and Nomura, H. (2017). Radiative grain alignment in protoplanetary disks: Implications for polarimetric observations. *Astrophys. J.* 839, 56. doi:10.3847/1538-4357/839/1/56
- Tercero, B., Cuadrado, S., López, A., Brouillet, N., Despois, D., and Cernicharo, J. (2018). Chemical segregation of complex organic O-bearing species in Orion KL. *Astron. Astrophys.* 620, L6. doi:10.1051/0004-6361/201834417
- Tram, L. N., Hoang, T., Soam, A., Lesaffre, P., and Reach, W. T. (2020). Modeling rotational disruption of grains and microwave emission from spinning dust in AGB envelopes. *Astrophys. J.* 893, 138. doi:10.3847/1538-4357/ab7b5e
- Tram, L. N., Hoang, T., Lee, H., Santos, F. P., Soam, A., Lesaffre, P., et al. (2021a). Understanding polarized dust emission from ρ ophiuchi A in light of grain alignment and disruption by radiative torques. *Astrophys. J.* 906, 115. doi:10.3847/1538-4357/abc6fe
- Tram, L. N., Hoang, T., Lopez-Rodriguez, E., Coudé, S., Soam, A., Andersson, B. G., et al. (2021b). SOFIA observations of 30 Doradus. I. Far-Infrared dust polarization and implications for grain alignment and disruption by radiative torques. *Astrophys. J.* 923, 130. doi:10.3847/1538-4357/ac13a1
- Tram, L. N., Lee, H., Hoang, T., Michail, J. M., Chuss, D. T., Nickerson, S., et al. (2021c). Observational evidence for rotational desorption of complex molecules by radiative torques from orion BN/KL. *Astrophys. J.* 908, 159. doi:10.3847/1538-4357/abcbe
- Tram, L. N., Bonne, L., Hu, Y., Lopez-Rodriguez, E., Guerra, J. A., Lesaffre, P., et al. (2022). *SOFIA observations of 30 Doradus: II – magnetic fields and large scale gas kinematics*. arXiv e-prints. arXiv:2205.12084.
- Tung, N.-D., and Hoang, T. (2020). Rotational disruption of dust and ice by radiative torques in protoplanetary disks and the implications for observations. *Astrophys. J.* 901, 6. doi:10.3847/1538-4357/abacbf
- van Dishoeck, E. F. (2014). Astrochemistry of dust, ice and gas: Introduction and overview. *Faraday Discuss.* 168, 9–47. doi:10.1039/C4FD00140K
- Vrba, F. J. (1977). Role of magnetic fields in the evolution of five dark cloud complexes. *Astron. J.* 82, 198–208. doi:10.1086/112031
- Whittet, D. C. B., Hough, J. H., Lazarian, A., and Hoang, T. (2008). The efficiency of grain alignment in dense interstellar clouds: a reassessment of constraints from near-infrared polarization. *Astrophys. J.* 674, 304–315. doi:10.1086/525040
- Wiesemeyer, H., Hezareh, T., Kreysa, E., Weiss, A., Güsten, R., Menten, K. M., et al. (2014). Submillimeter polarimetry with PolKa, a reflection-type modulator for the APEX telescope. *Publ. Astron. Soc. Pac.* 126, 1027–1047. doi:10.1086/679002
- Xu, Y., Moscadelli, L., Reid, M. J., Menten, K. M., Zhang, B., Zheng, X. W., et al. (2011). Trigonometric parallaxes of massive star-forming regions. VIII. G12.89+0.49, G15.03–0.68 (M17), and G27.36–0.16. *Astrophys. J.* 733, 25. doi:10.1088/0004-637x/733/1/25
- Zhang, Q., Qiu, K., Girart, J. M., Liu, H. B., Tang, Y.-W., Koch, P. M., et al. (2014). Magnetic fields and massive star formation. *Astrophys. J.* 792, 116. doi:10.1088/0004-637X/792/2/116
- Zielinski, N., Wolf, S., and Brunngräber, R. (2021). Constraining the magnetic field properties of Bok globule B335 using SOFIA/HAWC+. *Astron. Astrophys.* 645, A125. doi:10.1051/0004-6361/202039126